JOURNAL OF ENGINEERING RESEARCH & SCIENCES

JENRS

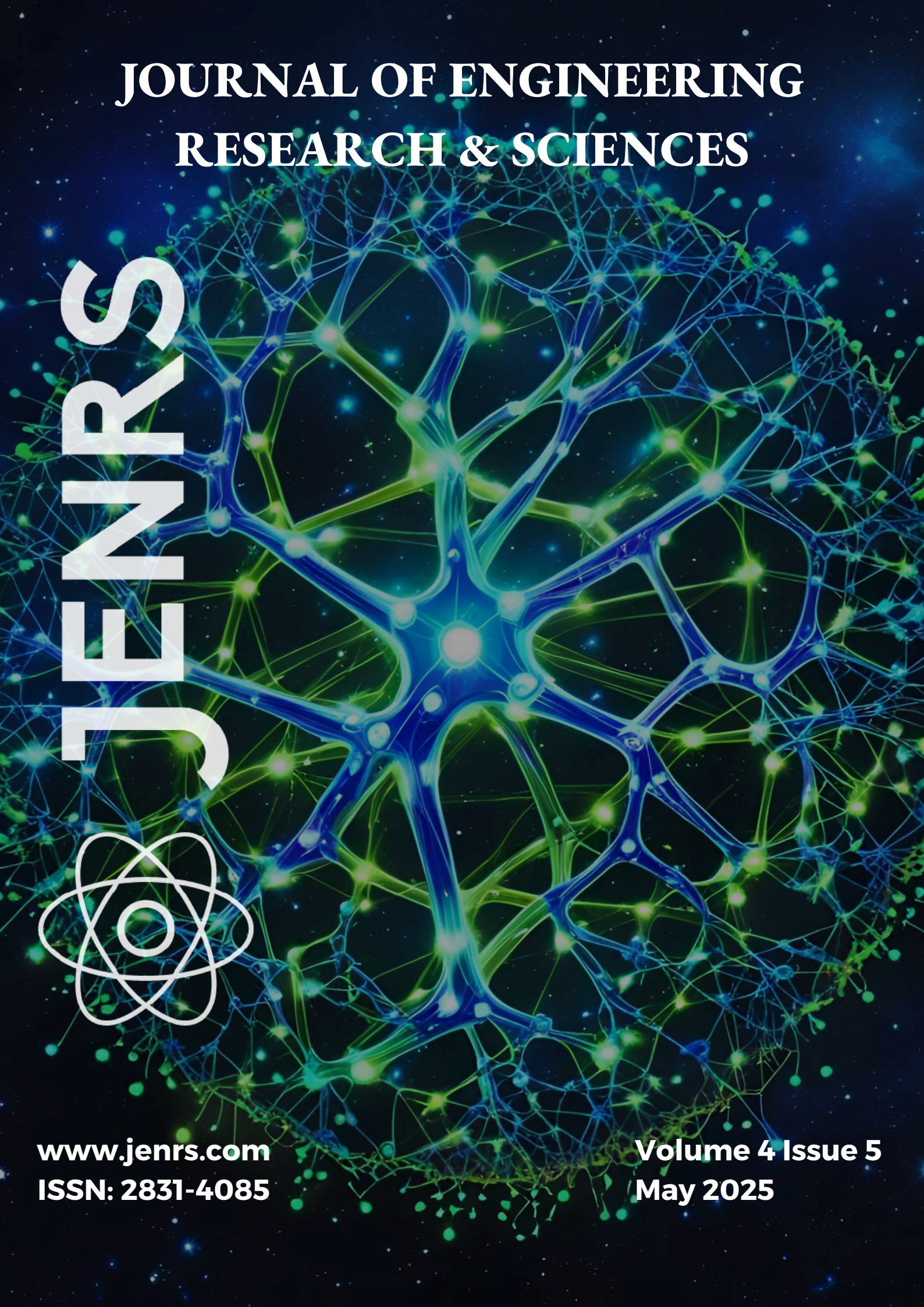

www.jenrs.com
ISSN: 2831-4085

Volume 4 Issue 5
May 2025

EDITORIAL BOARD

Editor-in-Chief

Editorial Board Members

Editorial

As technological innovation accelerates, research increasingly focuses on enhancing the performance, sustainability, and intelligence of modern systems across utilities, manufacturing, and energy infrastructure. The featured studies in this issue exemplify this progression, addressing critical challenges through advanced computational models, smart sensing, and reimagined energy transfer mechanisms. Whether optimizing water quality monitoring through deep learning, improving defect detection in manufacturing via in-mold sensors, or pioneering efficient power transmission through industrial repurposing, these contributions demonstrate the diverse potential of applied research in solving real-world problems.

Ensuring the potability of water is a growing concern amid rising levels of pollution and increased demand across multiple sectors. Addressing this, a comparative evaluation of Multilayer Perceptron (MLP) and Long Short-Term Memory (LSTM) neural networks was conducted to classify water quality using deep learning approaches. With a binary classification framework, the MLP model demonstrated exceptional accuracy and predictive power, achieving near-perfect scores across all major performance metrics including a 99.9% accuracy and a perfect ROC-AUC. These results markedly surpassed those of the LSTM model, reinforcing the suitability of MLP in water quality classification tasks. The study's outcomes present a highly efficient and reliable method for real-time water assessment, ensuring compliance with sector-specific potability standards and enabling prompt intervention when water quality deviates from acceptable thresholds [1].

In high-precision manufacturing environments, particularly injection molding, early defect detection is essential for ensuring consistent product quality and minimizing material waste. To address this, a real-time cavity monitoring system was developed using non-destructive in-mold sensors. The system takes into account part geometry to optimize sensor placement, enhancing the detection of abnormalities in regions prone to defects. A simulated case study using SolidWorks Plastics validated the proposed approach, with piezoelectric sensors achieving root mean square error values below 0.0004 V and peak errors of only 0.0012 V. These findings suggest a powerful enhancement to process monitoring, offering manufacturers better control over mold conditions and ultimately improving output quality and operational efficiency [2].

In the realm of transnational power distribution, leveraging existing infrastructure can offer innovative and cost-effective alternatives to traditional methods. A novel feasibility study explores the use of Oil & Gas (O&G) seabed piping infrastructure for high-voltage (HV) power transmission from Sarawak to Singapore. By suspending HV cables in the center of air-filled O&G pipes and using a return loop for air cooling, the setup aims to emulate the thermal dissipation properties of overhead lines, thereby overcoming the limitations of conventional submarine cables. Laboratory simulations involving current transmission up to 50 A across varying pipe diameters were conducted to measure eddy current-induced heat, with projections extended to currents of 1000 A. The findings highlight the potential for improved efficiency and reliability in long-distance power transmission using this unconventional yet practical approach [3].

Collectively, these studies illustrate the value of domain-specific innovation in addressing contemporary technological and environmental challenges. By integrating smart data-driven systems, intelligent infrastructure utilization, and precision engineering, the research featured here contributes to shaping more efficient, sustainable, and resilient solutions for tomorrow's global needs.

References:

[1] R. Taha, F. Musleh, A. Rahman Musleh, "Water Potability Prediction Using Neural Networks," *Journal of Engineering Research and Sciences*, vol. 4, no. 5, pp. 1–9, 2025, doi:10.55708/js0405001.

[2] O. Haberchad, "Cavity Sensing for Defect Prevention in Injection Molding," *Journal of Engineering Research and Sciences*, vol. 4, no. 5, pp. 11–20, 2025, doi:10.55708/js0405002.

[3] P. Karunakaran, M. Shahril Oaman, S. Sulaiman Maaji, C. Cheng Sung, "Electric Transmission from Sarawak to Singapore Using Cable Suspended within O&G Pipes," *Journal of Engineering Research and Sciences*, vol. 4, no. 5, pp. 20–33, 2025, doi:10.55708/js0405003.

Editor-in-chief

Dr. Jinhua Xiao

JOURNAL OF ENGINEERING RESEARCH AND SCIENCES

Volume 4 Issue 5 May 2025

CONTENTS

Received: 13 January, 2025 Revised: 02 March, 2025 Accepted: 03 March, 2025 Online: 20 May, 2025

DOI: https://doi.org/10.55708/js0405001

Water Potability Prediction Using Neural Networks

Ranyah Taha[*,1], **Fuad Musleh**[2], **Abdel Rahman Musleh**[3]

[1] Computer Science Dept., Al-Iman School, Bahrain

[2] Civil engineering Department, College of Engineering, University of Bahrain, Sakhir, 1054, Bahrain

[3] Electrical and Electronics Engineering Department, College of Engineering, University of Bahrain, Sakhir, 1054, Bahrain

*Corresponding author: Ranyah Taha, raniacs2014@gmail.com

ABSTRACT: The crucial need for maintaining specific water potability levels depending on the sector of utilization, this is becoming increasingly challenging due to the increased pollution. It is therefore important to have fast and reliable water potability assessment techniques. A subset of Machine Learning (ML); being Deep Learning (DL), can be utilized to develop models capable of measuring water quality while assessing its potability with high levels of accuracy; thus, ensuring that water meets the set standards based on the required sector of utilization. In this research, the effectiveness of Multilayer Perceptron (MLP) and Long Short-Term Memory (LSTM) Neural Networks (NN) were contrasted for Water Quality Classification (WQC). The MLP model demonstrated superior performance, achieving higher precision, accuracy, F-measure, recall and the area under the receiver operating characteristic curve (ROC-AUC) scores, indicating its effectiveness in this application compared to the LSTM approach. The experimental findings revealed that MLP NN model outperformed the LSTM NN model in WQC tasks. The MLP model achieved very high performance with an accuracy of 99.9%, an F-measure of 99.9%, a precision of 99.9%, a recall of 99.9%, and a ROC-AUC of 100%, significantly outperforming the LSTM model, which attained an accuracy of 97.6%, an F-measure of 97.1%, a precision of 97.1%, a recall of 97.5%, and a ROC-AUC of 97.9%. The study's novelty lies in employing DL for binary classification, yielding outstanding outcomes in the crucial domain of WQC.

KEYWORDS: Artificial Intelligence, Data Analysis, Water Quality Classification, Neural Networks, Civil Engineering.

1. Introduction

Water is the main and fundamental component in all biological processes; hence, it is the principal element crucial for sustaining all forms of life and a balanced ecosystem. Additionally, being in the industrial age, water became vital in a range of manufacturing processes; moreover, as time goes water is introduced into further domains; therefore, increasing the water demand necessary to sustain all these applications [1].

As this demand for water increases the issue of water scarcity even grows deeper; this is because of the lack of clean, directly utilizable water sources; in addition to, the continued pollution of water sources due to unresponsible human behavior. This dictates water treatment processes that transform contaminated water into untainted water. The overlapping of water into a variety of domains means that there is a spectrum of water quality levels depending on the sector [2].

Water quality and potability are closely related, as evaluating water quality involves assessing its appropriateness based on its physical, chemical, and biological attributes for different uses. Potability specifically focuses on whether water is safe for human consumption, ensuring it meets health standards and is free from harmful contaminants. Water quality refers to the overall status of water as reflected through its biological, chemical, and physical characteristics, determining its suitability for various uses, such as agriculture or industrial processes. The differences between them affect their assessment techniques: water quality assessments may include a broader range of tests for pollutants and environmental impact, while potability focuses on specific contaminants and health-related criteria to ensure drinking safety. Understanding these distinctions is crucial for effective water management and public health [2].

Conventional methods have been employed to evaluate water quality, particularly to ascertain its potability; however, these traditional approaches can now be replaced by new procedures that ensure higher accuracy and precision. These new techniques are equipped with the usage of Artificial Intelligence (AI) and specifically the usage of DL, a branch of ML [3].

Machine learning incorporates the utilization of mathematical models that can identify the trends and characteristics through which water is classified into contaminated or untainted depending on the domain. Thus, through a range of variables, water quality and water potability are instantly assessed and classified with nearly faultless accuracy [3].

This study seeks to assess and compare the potency of two Neural Network (NN) architectures, LSTM and MLPs, for WQC; NNs are the fundamental components of DL. The study will abide by the Cross-Industry Standard Protocol for Data Mining (CRISP-DM) methodology working on a dataset obtained from a government-maintained official website in India.

The upcoming segments of this article will be organized beginning with literature review, followed by methodology, description and preparation of the dataset, moving on to the classification algorithm, the outcomes, and concluding with both the discussion and the conclusion.

2. Literature Review

Due to the significance of the topic, much research has been targeted at the topic of water potability forecasting. This section will highlight some of these contributions to set a scientific base for comparison with the results obtained in this work.

To start, a study conducted by [4] investigates the applicability of AutoDL in Water Quality Assessment. AutoDL is an emerging field, automating DL pipelines; subsequently, comparing its performance against conventional models. Results show that conventional DL outperforms AutoDL by 1.8% for binary class data and 1% for multiclass data, with accuracies ranging from ~96% to ~99%.

Additionally, In [5], the authors carried a study focused on forecasting water's quality in one of Greece's lakes, conventional ML models such as Support Vector Regression (SVR) and Decision Tree (DT) were pitted against DL models like LSTM, Conventional Neural Network (CNN), and a hybrid CNN-LSTM model. The objective was to predict levels of Chlorophyll-a (Chl-a) and Dissolved Oxygen (DO) using physicochemical variables collected between June 2012 and May 2013. The novel merged approach showed improved performance over standalone models. Lag times of up to two intervals were used for prediction. LSTM excelled in DO prediction, while both DL models performed similarly for Chl-a. The merged CNN-LSTM approach demonstrated superior predictive accuracy for both variables, effectively capturing variations in DO concentrations. Evaluation metrics included correlation coefficients, RMSE, MAE, and graphical analyses, revealing the hybrid model's enhanced predictive capabilities in capturing diverse water quality levels.

Moreover, research proposed by [6] addresses the precise estimation of Effluent Total Nitrogen (E-TN) for optimizing the operations of Wastewater Treatment facilities (WWTPs), ensuring regulatory compliance and reducing energy usage. The complexity inherent in WWTPs poses a significant obstacle for accurate multivariate time series forecasting of E-TN due to their intricate nonlinear nature. To tackle this challenge, a new predictive framework is proposed, integrating the Golden Jackal Optimization (GJO) algorithm for feature selection and a hybrid DL architecture, the CNN-LSTM-TCN (CLT) model. CLT combines CNN, LSTM, and TCN to capture complex interrelations within WWTP datasets. A two-step feature selection process enhances prediction precision, with GJO fine-tuning CLT hyperparameters. Findings underscore the effectiveness of the proposed system in precisely forecasting multivariate water quality time series in WWTPs, demonstrating superior performance across diverse prediction scenarios.

In this study performed by [7] supervised learning is utilized to develop precise predictive models from labeled data, aiming to categorize water as safe or unsafe based on its characteristics. Various ML models are assessed for binary classification using features like physical, chemical, and microbial parameters. The findings demonstrate that the Stacking model, in combination with SMOTE and 10-fold cross-validation, it surpasses other methods, yielding remarkable outcomes. Notably, it demonstrates an accuracy and recall rate of 98.1%, precision of 100%, and an AUC value of 99.9%.

Furthermore, a study by [8] introduces a merged IoT and ML system for detailed water quality forecasting. By analyzing Rohri Canal data in SBA, Pakistan, the system predicts Water Quality Class and Water Quality Index (WQI). ML models like LSTM, SVR, MLP, and Nonlinear Autoregressive Neural Network (NARNet) predict WQI, while Support Vector Machine (SVM), Extreme Gradient Boosting (XGBoost), DT, and Random Forest (RF) forecast WQC. Results indicate that the MLP regression model excels with the lowest errors and highest R-squared (R2) of 0.93. RF leads in classification, achieving high precision (0.93), accuracy (0.91), recall (0.92), and a F1-score of 0.91. Notably, models perform better with smaller datasets. This study demonstrates enhanced regression and classification performance compared to previous research.

In another study conducted by [9] a system combining a Discrete Wavelet Transform (DWT), LSTM, and an Artificial Neural Network (ANN) was created to predict the Jinjiang River's water quality. Initially, a MLP-NN handled missing values within the water quality dataset. Subsequently, the Daubechies 5 (Db5) wavelet divided the data into low and high-frequency signals, serving as LSTM inputs for training and prediction. Comparative analysis against various models such as NAR, Autoregressive Integrated Moving Average (ARIMA), ANN-LSTM, MLP, LSTM, and CNN-LSTM demonstrated the superior performance of the ANN-WT-LSTM model across multiple evaluation n metrics, highlighting its effectiveness in the forecasting of the quality of water.

To evaluate the efficacy of the proposed DL method incorporating LSTM, Gated Recurrent Unit (GRU), and Recurrent Neural Network (RNN) a case study was undertaken in a southern Chinese city by [10]. A comparison was made between the proposed method, a linear approach which is the Multiple Linear Regression, (MLR), and a traditional learning algorithm (MLP). The DL algorithm demonstrated strong predictive capabilities, with GRU outperforming in predicting water quality chemical indices and exhibiting a swifter learning curve. Findings indicated that GRU outperformed traditional ML algorithms by 9.13%–15.03% in terms of R2, surpassed RNN and LSTM by 0.82%–5.07%, and exceeded linear methods by 37.26%–43.38% for the same parameter.

Moving forward, in a study proposed by [11] a novel system for monitoring drinking water potability, emphasizing sustainability and environmental friendliness was introduced. An adaptive neuro-fuzzy inference system (ANFIS) was created for WQI prediction, while K-nearest neighbors (KNN) and Feed-forward neural network (FFNN) were utilized for WQC. The ANFIS model excelled in WQI prediction, while the FFNN algorithm achieved 100% accuracy in WQC. Notably, ANFIS demonstrated 96.17% accuracy in WQI prediction during testing, while FFNN remained robust in classifying water quality.

In the research led by [12], sophisticated AI algorithms were formulated to forecast the Water Quality Index (WQI) and categorize water quality. SVM, K-NN, and Naive Bayes algorithms were utilized for Water Quality Classification (WQC) forecasting while NARNet and LSTM DL models were applied for WQI prediction. The assessment of the models, based on statistical metrics, was conducted using a dataset featuring 7 key parameters, showcasing their accuracy in predicting WQI and classifying water quality effectively. Results indicated that NARNET slightly outperformed LSTM in WQI prediction, while SVM achieved the highest WQC prediction accuracy with 97.01%. During testing, LSTM and NARNET showed close accuracies with slight differences in regression coefficients with 96.17% and 94.21% respectively.

Finally, in a study conducted by [13] ML models were trained using the Water Quality dataset sourced from the Indian Government website via Kaggle. The WQI served as the basis for data categorization. Various ML algorithms, including DTs, MLP, XGBoost, KNN, and SVM, were investigated. To evaluate model effectiveness, metrics including Precision, Recall, Accuracy, and F1-Score were utilized. Results indicated that XGBoost exhibited superior performance as a water quality classifier, boasting an accuracy of 95.12%, closely followed by SVM with an accuracy of 93.22%.

While DL and ML approaches have proven effective in water quality assessment, several limitations exist in prior work. AutoDL, despite its automation, struggles with domain-specific optimizations, as conventional models outperform it by 1.8% in binary classification and 1% in multiclass classification. Additionally, model comparisons often lack robust justification, as seen in Barzegar et al., where SVR, DT, LSTM, CNN, and CNN-LSTM were analyzed for specific water quality parameters without evaluating fully connected architectures like MLP, which have shown strong performance in another research.

Furthermore, hybrid models like CLT introduce additional computational complexity, requiring feature selection via the GJO algorithm, making them less practical for real-time water monitoring. Similarly, supervised learning approaches using SMOTE, as in Dritsas and Trigka, achieve high accuracy (98.1%) but risk bias due to synthetic data introduction. Prior research highlights MLP's strength in regression tasks, with Najah et al. reporting an R^2 of 0.93, outperforming other models, while Wu and Wang demonstrated MLP's effectiveness in handling missing data alongside LSTM's ability to process sequential dependencies. Moreover, Jiang et al. showed that GRU outperformed LSTM and traditional ML models by 9.13%-15.03% in R^2, reinforcing the effectiveness of recurrent models for time series water quality prediction. These findings emphasize the need for a more balanced evaluation of model architectures, computational feasibility, and data augmentation risks in future research.

3. Research Methodology and approach

3.1. Background of the Research Study

Google collab was the platform for conducting this study; moreover, ML libraries in python called keras and Scikit-learn were used in the programming phase. Moreover, two ML techniques being LSTM, and MLP

were used on the dataset. This study followed a six-phase methodology, which is CRISP-DM [14].

Figure 1. Phases of the CRISP-DM Methodology.

3.2. *Dataset Description*

The dataset focuses on water quality (WQ) parameters in India, collected between 2012 and 2021. Data was gathered from an authorized Indian government website, comprising 7339 entries with six attributes per entry and a solitary outcome variable [15]. A breakdown of these attributes is detailed in Table 1.

When evaluating water drinkability various essential factors were considered, such as Biochemical Oxygen Demand (BOD), electrical conductivity (EC), pH, DO, and total coliforms (TC). A WQI is calculated using these parameters to provide a comprehensive evaluation of water potability. The WQI calculation involves deriving new parameters from the original measurements using a specific classification system. These derived parameters are denoted as ndo, nco, nbdo, nec, npH, and nna, representing normalized values for pH, DO, TC, BOD, EC, and NA. Weighted averages are then calculated for each parameter using the following formulas shown in equation (1-7) [15]:

- Weighted contribution for pH is given by:

$$wph = nph * 0.165 \quad (1)$$

- Weighted contribution for DO is given by:

$$wdo = npo * 0.281 \quad (2)$$

- Weighted contribution for Biochemical Oxygen Demand (BOD) is given by:

$$wbdo = nbdo * 0.234 \quad (3)$$

- Weighted contribution for Electrical Conductivity (CE) is given by:

$$wec = nec * 0.009 \quad (4)$$

- Weighted contribution for Sodium (NA) is given by:

$$wna = nna * 0.028 \quad (5)$$

- Weighted contribution for Total Coliform (TC) is given by:

$$wco = nco * 0.281 \quad (6)$$

- The Final Water Quality Index (WQI) is

Calculated using the formula:

$$\text{WQI} = wph + wdo + wbdo + wec + wna + wco \quad (7)$$

Water samples are categorized as drinkable (1) when the WQI equals or exceeds 75, and undrinkable (0) if the WQI falls below 75. This method of classification offers a uniform method for evaluating water suitability using defined benchmarks and measured concentrations.

Table 1. Dataset Description

Attribute	Description	Datatypes
Dissolved Oxygen (DO)	Optimum DO Concentration is 10 mg/L.	float64
pH	The required pH is 8.5.	float64
Conductivity (EC)	The wanted Conductivity is 1,000 µS/cm.	float64
Biological Oxygen Demand (BOD)	The optimum concentration is 5 mg/L.	float64
Nitrate (NA)	The optimum concentration is 45 mg/L.	float64
Total coliform (TC)	The required value is 100 per 100 mL	float64
Potability	A rating of 1 indicated that the water is safe to drink, while a rating of 0 means it is not safe to drink.	object

3.3. *Dataset Preparation*

After examining the data, the next step is to prepare it for analysis and model building. This involves addressing missing data, transforming categorical variables into numerical values, and dividing the dataset into appropriate testing and training subsets.

3.3.1. *Missing Data*

In this study, two essential functions commonly used to check for missing or duplicated data in a dataset, isnull().sum() and duplicated().sum(), were applied to ensure data integrity. The isnull().sum() function identifies and counts missing values in each column, while duplicated().sum() detects redundant rows. After executing these functions, the results confirmed that there were no missing or duplicated data, affirming the dataset's completeness and consistency. This ensures higher data quality, ultimately enhancing the reliability and accuracy of the ML model.

3.3.2. *Balancing the Dataset*

The value counts () function was used to assess class balance, revealing 3,958 instances for class 0 and 3,381 instances for class 1. A dataset is typically considered imbalanced if one class significantly outweighs the other.

To quantify this, the imbalance ratio was calculated as 3958 / 3381 ≈ 1.17, indicating that the dataset is relatively balanced. Generally, datasets with imbalance ratios exceeding 1.5–2.0 are considered imbalanced and may require techniques such as SMOTE (Synthetic Minority Over-sampling Technique) or undersampling to correct class distribution.

3.3.3. *Encoding Categorical Data*

The LabelEncoder function was applied to the dataset to convert categorical data into numerical values, a crucial step for preparing data for ML models, which typically require numerical inputs. In this study, water samples were classified based on the WQI, where a value of 75 or higher indicated potable water (labeled as 1), while a WQI below 75 signified non-potable water (labeled as 0). This transformation ensures that the dataset is properly formatted for model training therefore enhancing the efficiency of the classification process [16].

3.3.4. *Splitting Data*

To assess the capabilities of the algorithms at water potability forecasting, the study employed a 10-fold cross-validation approach. This method ensured a robust *assessment of the algorithms, improving the generalizability and reliability of the research discoveries [17].*

3.3.5. *Data Normalization*

The numerical data was normalized to scale values within a predefined range, typically 0 to 1 or -1 to 1, ensuring uniform feature contribution. This transformation prevents any single variable from dominating the model, promoting balanced and unbiased learning.

3.4. *Modelling*

The two NNs, MLP and LSTM are implemented to predict water potability.

MLPs: a type of ANN, excel at solving complex classification and regression tasks. These networks are structured as layers of interconnected nodes, each processing information and relaying it to the next layer. The network learns by fine-tuning the connections between nodes, enabling it to recognize complex patterns within data. MLPs are particularly adept at handling non-linear relationships and can be trained to achieve high accuracy across a wide range of applications [18].

In this study The MLP model had been configured with 2-3 hidden layers, with each layer having 64, 128, or 256 neurons, depending on the complexity of the task. The activation functions used had been ReLU for the hidden layers to facilitate efficient training and Sigmoid for the output layer to support binary classification. The Adam optimizer had been selected for its adaptive learning properties, while the Binary Crossentropy loss function had been utilized to optimize performance for the binary classification task. The batch size had been set to 64 to balance computational efficiency and memory usage. The model had been trained over 50 to 100 epochs, with a learning rate of 0.001 to ensure stable convergence. Additionally, dropout rates between 0.2 and 0.3 had been applied to prevent overfitting during training.

LSTM: a type of RNN, designed to handle sequential data. Unlike traditional RNNs, it utilizes a unique memory cell structure that allows them to retain information over extended periods. This renders them well-suited for assignments encompassing natural language processing, time series analysis, and speech recognition. LSTMs' ability to "remember" past information enables them to grasp extended dependencies within sequences, leading to improved accuracy in predicting future outcomes [19].

In this study the LSTM model had been configured using a network architecture comprising 1-2 LSTM layers followed by a Dense layer. The number of units (neurons) in each LSTM layer had ranged from 64 to 256, depending on the data's complexity. The activation functions used had been Tanh for the LSTM layers and Sigmoid for the output layer, facilitating efficient learning and binary classification. The Adam optimizer had been employed for its adaptive learning capabilities, paired with the Binary Cross entropy loss function for optimizing binary classification tasks. The batch size had been set to 64, balancing memory usage and computational efficiency. The model had been trained over 50 to 100 epochs, with dropout rates between 0.2 and 0.5, and recurrent dropout rates ranging from 0.2 to 0.3 to reduce overfitting. Finally, the learning rate had been set to 0.001 to ensure steady convergence during training.

3.5. *Performance Evaluation*

The capabilities of the NNs are identified through accuracy, sensitivity, precision, and ROC-AUC are all used to measure their performance.

3.5.1. *Accuracy:*

This metric represents the portion of true forecast by a model out of all predictions made as shown in equation (8) [20].

$$Accuracy = \frac{TP + TN}{TP + TN + FP + FN} \quad (8)$$

3.5.2. *F-measure:*

The F-measure provides an equitable evaluation of a model's precision and recall. It calculates a weighted average of these two metrics, providing an extensive assessment of the model's capabilities shown in equation (9) [21].

$$F - measure = 2 \times \frac{precision \times recall}{precision + recall} \quad (9)$$

3.5.3. ROC-AUC Value:

It evaluates a classification model's performance across various threshold settings. The AUC indicates the model's ability to distinguish between classes, and higher ROC-AUC scores signify improved classification performance and discriminative capacity [21].

3.5.4. Precision:

It assesses the ratio of accurately identified negative instances (true negatives) among all cases predicted as negative shown in equation (10) [21].

$$Precision = \frac{TP}{TP + FP} \quad (10)$$

3.5.5. Recall:

It evaluates a model's capacity to accurately detect all positive instances present in a dataset shown in equation (11) [21].

$$Recall = \frac{TP}{TP + FN} \quad (11)$$

4. Results

The experimental findings revealed that MLP NN model outperformed the LSTM NN model in WQC tasks. The MLP model achieved a near-perfect accuracy of 99.9%, significantly higher than the 97.6% accuracy of the LSTM model. This suggests that the MLP is more reliable in correctly classifying the water potability samples.

The MLP's F-measure of 99.9% surpasses the LSTM's 97.1%. Recall and Precision for the MLP model are near perfect at 99.9%, indicating that the MLP has a very low false positive and false negative rate. The LSTM, while still performing well, shows slightly lower precision (97.1%) and recall (97.5%), suggesting it is less effective in minimizing these errors as shown in Table II and Figure 2.

This ROC-AUC curve comparison highlights the classification performance of the MLP and LSTM models. The MLP model achieves a perfect AUC of 100%, represented by a diagonal line, indicating flawless classification, whereas the LSTM model attains an AUC of 97.9%, demonstrating strong but slightly lower performance as shown in Figure 3.

Table 2. Performance Comparison between NNs.

Models	MLP	LSTM
Accuracy	99.9%	97.6%
F-measure	99.9%	97.1%
Precision	99.9%	97.1%
Recall	99.9%	97.5%
ROC-AUC	100%	97.9%

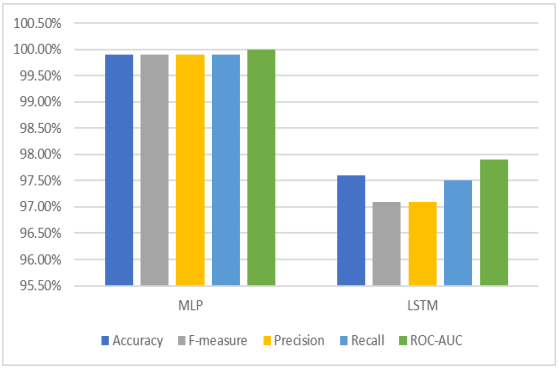

Figure.2: Performance Plot of Proposed Neural Networks

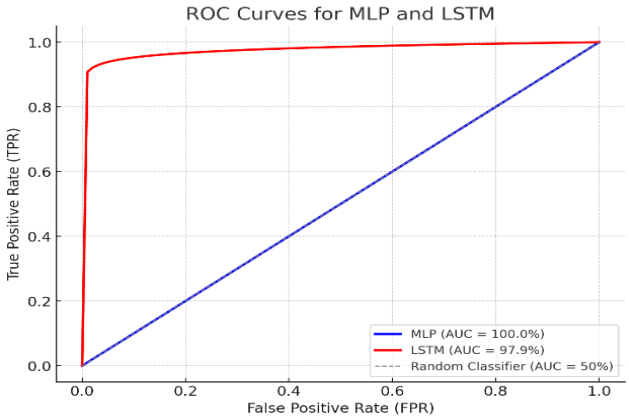

Figure.3: The ROC-AUC Plot of Proposed Neural Networks

5. Discussion

The current study demonstrates the superiority of MLP over LSTM for binary water potability classification, with MLP achieving 99.9% across all metrics, outperforming results from prior studies. Compared to Prasad et al., who found conventional DL models achieving up to 99% accuracy, and Dritsas and Trigka, whose stacking model reached 98.1%, the MLP model's perfect ROC-AUC of 100% sets a new benchmark. While LSTM performed slightly below MLP in this study, previous research, such as by Barzegar et al. and Liu et al., highlights LSTM's strength in multivariate and temporal tasks, particularly in hybrid architectures like CNN-LSTM and CLT. Studies like Najah et al. and Wu and Wang reaffirm MLP's excellence for regression and classification tasks, and the current study underscores its efficiency for simpler tasks without relying on hybrid approaches or extensive preprocessing. This suggests that while LSTM excels in capturing temporal dependencies, MLP's straightforward architecture is more effective for binary classification.

Many previous studies have focused on multi-class classification or regression-based approaches to predict the WQI rather than directly classifying water as potable or non-potable. For instance, Liu et al. employed a hybrid CLT model to predict multivariate water quality parameters, concentrating on continuous values instead of binary classification. Similarly, Barzegar et al. used a CNN-LSTM hybrid model to predict DO and Chl-a levels rather than focusing on binary classification. These models require additional steps to convert their outputs into potable/non-potable labels, adding unnecessary complexity and potential misclassification risks. Consequently, there is a need for direct binary classification models that efficiently determine water potability. The current research explicitly focuses on binary classification, optimizing the process for direct decision-making and achieving a near-perfect accuracy of 99.9% using the ML model.

Many prior studies have also overcomplicated their models by integrating multiple DL architectures (e.g., CNN-LSTM, ANN-WT-LSTM) under the assumption that this will enhance predictive accuracy. Wu and Wang, for example, used a hybrid ANN-Wavelet Transform-LSTM model, significantly increasing computational complexity. Similarly, Najah et al. combined IoT with ML models such as LSTM, SVR, MLP, and NARNet for WQI prediction, instead of opting for a simpler and more effective classifier. These hybrid models tend to be computationally expensive, require extensive hyperparameter tuning, and lack interpretability, making them impractical for real-time applications. Additionally, many studies fail to demonstrate whether the added complexity truly results in better performance than simpler models like MLP. In contrast, the current research demonstrates that a straightforward MLP model can outperform LSTM, achieving an accuracy of 99.9% compared to LSTM's 97.6%, without requiring hybrid architectures.

Another major limitation in prior work is the neglect of feature selection and data preprocessing. Some studies feed raw data directly into DL models without conducting proper feature selection or normalization. For example, Liu et al. applied GJO for feature selection, but many other studies lacked systematic feature engineering. The absence of feature selection can lead to overfitting and reduced generalizability. Moreover, many prior works do not systematically explore how feature normalization or selection impacts model performance. The current study addresses this gap by applying proper feature engineering, ensuring that only the most relevant attributes contribute to model performance, thereby improving accuracy and efficiency.

Additionally, many studies have overlooked traditional ML models, assuming that DL models always perform better. For instance, Aldhyani et al. compared SVM, KNN, and Naïve Bayes with DL models, but many other studies did not conduct such benchmarking. Traditional ML models, such as DT, RF, and SVM, can sometimes perform equally well or even better than DL models, particularly with smaller datasets. Many studies fail to justify why DL is necessary over simpler, more explainable models. In contrast, the current study provides a clear justification for using DL.

The superior performance of MLP over LSTM in this study can be attributed to the nature of the task and the architectural differences between the two models. MLP, being a feedforward NN, is well-suited for binary classification tasks where the data lacks significant temporal dependencies. Its simpler architecture focuses on mapping inputs directly to outputs through fully connected layers, enabling efficient learning of non-linear relationships in static datasets.

By critically analyzing prior work, the selection of MLP and LSTM had been justified as offering high predictive accuracy, robust performance in both regression and classification tasks, and efficient processing for multivariate tabular data and time-series forecasting. Additionally, better scalability for real-world applications had been provided compared to computationally expensive hybrid models. The ability to handle both static and sequential data effectively while outperforming existing DL models in accuracy and efficiency had made them optimal choices for water quality assessment.

6. Conclusion a Future Direction

The results clearly demonstrate the inferior performance of the LSTM model contrasted to the superior MLP model in water potability classification. Across all metrics, the MLP consistently outperforms the LSTM, achieving near-perfect scores for accuracy, F-measure, precision, recall, and a perfect ROC-AUC score. This suggests that the MLP's architecture is more fitted for capturing the intricate relationships and patterns present in the datasets concerning water potability, leading to more precise predictions.

This study highlights the crucial role of NNs in classification processes, particularly for complex datasets like those found in water potability analysis. NNs, utilizing their capability to comprehend intricate patterns and adjust to non-linear connections, offer a powerful tool for tackling such challenges. The MLP's superior performance in this instance underscores the importance of selecting the right NN architecture for the specific task since each model excel in different domains.

Future research can advance water potability classification by integrating hybrid DL models, such as

combining MLP with CNN or Transformer-based architecture, to enhance feature extraction and classification accuracy. Utilizing advanced feature selection techniques, including genetic algorithms and particle swarm optimization, can further refine model performance. Expanding from binary to multi-class classification would allow for a more detailed evaluation of water quality levels. Implementing IoT-enabled real-time monitoring systems can enable continuous water quality tracking and instant alerts when contamination exceeds safety thresholds. Additionally, incorporating spatiotemporal analysis using GIS and remote sensing data can improve predictive capabilities. Exploring diverse datasets from various geographical regions and environmental conditions would enhance model robustness, ensuring its applicability across different water sources and pollution levels.

Conflict of Interest

The authors declare no conflict of interest.

Acknowledgment

The Authors hereby acknowledge that the funding of this paperwork was done and shared across all Authors concerned.

References

[1] J. J. Bogardi, J. Leentvaar, and Z. Sebesvári, "Biologia Futura: integrating freshwater ecosystem health in water resources management," *Biologia futura*, vol. 71, no. 4, pp. 337-358, 2020, DOI: doi.org/10.1007/s42977-020-00031-7.

[2] N. I. Obialor, "The Analysis of Water Pollution Control Legislation and Regulations in Nigeria: Why Strict Implementation and Enforcement Have Remained a Mirage," *Available at SSRN 4600394*, 2023.

[3] R. Huang, C. Ma, J. Ma, X. Huangfu, and Q. He, "Machine learning in natural and engineered water systems," *Water Research*, vol. 205, p. 117666, 2021, DOI: 10.1016/j.watres.2021.117666.

[4] D. V. V. Prasad *et al.*, "Analysis and prediction of water quality using deep learning and auto deep learning techniques," *Science of the Total Environment*, vol. 821, p. 153311, 2022, DOI: 10.1016/j.scitotenv.2022.153311.

[5] R. Barzegar, M. T. Aalami, and J. Adamowski, "Short-term water quality variable prediction using a hybrid CNN–LSTM deep learning model," *Stochastic Environmental Research Risk Assessment*. vol. 34, no. 2, pp. 415-433, 2020, doi.org/10.1007/s00477-020-01776-2.

[6] W. Liu, T. Liu, Z. Liu, H. Luo, and H. Pei, "A novel deep learning ensemble model based on two-stage feature selection and intelligent optimization for water quality prediction," *Environmental Research*, vol. 224, p. 115560, 2023, DOI: 10.1016/j.envres.2023.115560.

[7] E. Dritsas and M. Trigka, "Efficient data-driven machine learning models for water quality prediction," *Computation*, vol. 11, no. 2, p. 16, 2023, DOI: 10.3390/computation11020016.

[8] A. Najah, A. El-Shafie, O. A. Karim, and A. H. El-Shafie, "Application of artificial neural networks for water quality prediction," *Neural Computing Applications*,vol. 22, pp. 187-201, 2013, DOI: 10.1007/s00521-012-0940-3.

[9] J. Wu and Z. Wang, "A hybrid model for water quality prediction based on an artificial neural network, wavelet transform, and long short-term memory," *Water*, vol. 14, no. 4, p. 610, 2022, DOI: 10.3390/w14040610.

[10] Y. Jiang, C. Li, L. Sun, D. Guo, Y. Zhang, and W. Wang, "A deep learning algorithm for multi-source data fusion to predict water quality of urban sewer networks," *Journal of Cleaner Production*, vol. 318, p. 128533, 2021, DOI: 10.1016/j.jclepro.2021.128533.

[11] M. Hmoud Al-Adhaileh and F. Waselallah Alsaade, "Modelling and prediction of water quality by using artificial intelligence," *Sustainability*, vol. 13, no. 8, p. 4259, 2021, DOI: 10.3390/su13084259.

[12] T. H. H. Aldhyani, M. Al-Yaari, H. Alkahtani, and M. Maashi, " Water Quality Prediction Using Artificial Intelligence Algorithms," *Applied Bionics Biomechanics*, vol. 2020, no. 1, p. 6659314, 2020, DOI: 10.1155/2020/6659314.

[13] J. Kirui, "Machine Learning Models for Drinking Water Quality Classification," in *2024 International Conference on Control, Automation and Diagnosis (ICCAD)*, 2024, pp. 1-5: IEEE, DOI: 10.1109/ICCAD60883.2024.10553712.

[14] A. M. Zeki, R. Taha, and S. Alshakrani, "Developing a predictive model for diabetes using data mining techniques," in *2021 International Conference on Innovation and Intelligence for Informatics, Computing, and Technologies (3ICT)*, 2021, pp. 24-28: IEEE, DOI: 10.1109/3ICT53449.2021.9582114.

[15] F. Ahmad Musleh, "A Comprehensive Comparative Study of Machine Learning Algorithms for Water Potability Classification," *International Journal of Computing Digital Systems*,,vol. 15, no. 1, pp. 1189-1200, 2024, DOI:10.12785/ijcds/150184.

[16] R. Taha, S. Alshakrani, and N. Hewahi, "Exploring Machine Learning Classifiers for Medical Datasets," in *2021 International Conference on Data Analytics for Business and Industry (ICDABI)*, 2021, pp. 255-259: IEEE, DOI: 10.1109/ICDABI53623.2021.9655862.

[17] S. M. Malakouti, M. B. Menhaj, and A. A. Suratgar, "The usage of 10-fold cross-validation and grid search to enhance ML methods performance in solar farm power generation prediction," *Cleaner Engineering Technology*,vol. 15, p. 100664, 2023, DOI: 10.1016/j.clet.2023.100664.

[18] S. Afzal, B. M. Ziapour, A. Shokri, H. Shakibi, and B. Sobhani, "Building energy consumption prediction using multilayer perceptron neural network-assisted models; comparison of different optimization algorithms," *Energy*, vol. 282, p. 128446, 2023, DOI: 10.1016/j.energy.2023.128446.

[19] K. Li, W. Huang, G. Hu, and J. Li, "Ultra-short term power load forecasting based on CEEMDAN-SE and LSTM neural network," *Energy Buildings*,vol. 279, p. 112666, 2023, DOI: 10.1016/j.enbuild.2022.112666.

[20] F. Musleh, R. Taha, and A. R. Musleh, "Comparative Analysis of Machine Learning Techniques for Concrete Compressive Strength Prediction," in *2023 4th International Conference on Data Analytics for Business and Industry (ICDABI)*, 2023, pp. 146-151: IEEE, DOI: 10.1109/ICDABI60145.2023.10629479.

[21] F. A. Musleh and R. G. Taha, "Forecasting of forest fires using machine learning techniques: a comparative study," 2022, DOI: 10.1049/icp.2023.0571.

Mrs. Ranyah Taha completed her MSc in Big Data Science and Analytics in 2022 through a joint program between Liverpool John Moores University and the University of Bahrain. She earned her BSc in Computer Science from the University of Bahrain in 2018. Her research focuses on leveraging Data Science and Analytics, particularly Machine Learning and Deep Learning, to build advanced models and extract valuable insights from complex datasets. She has contributed to many research papers and was awarded the NASA International Space Apps Challenge – Space Apps Bahrain 2023 Local Impact Award and the Second Prize for Best Use of Satellite Data in the competition held by the NSSA in celebration of the launch of Bahrain's first satellite, Al Munther.

Dr. Fuad Musleh is an Assistant Professor at the University of Bahrain. He received his Ph.D. and MSc degrees from the University of Alabama in Huntsville, B.Sc. from Jordan University of Science and Technology in Jordan. He is interested in research related to flow through vegetation, water and environmental conservation. Additionally, he is interested in leveraging Data Analysis in his field.

Mr. Abdel Rahman Musleh is a Senior BSc in Electrical Engineering student at the University of Bahrain, with an interest in leveraging AI and ML to develop Cyber-Physical Systems that enhance efficiency, reliability, and sustainability.

Received: 04 April, 2025, Revised: 07 May, 2025, Accepted: 15 May, 2025, Online: 25 May, 2025

DOI: https://doi.org/10.55708/js0405002

Cavity Sensing for Defect Prevention in Injection Molding

Oumayma Haberchad [*1], **Yassine Salih-Alj** [2]

[1] Control and Instrumentation Engineering Department, College of Engineering and Physics, King Fahd University of Petroleum and Minerals, Dhahran, 31261, Saudi Arabia

[2] School of Science and Engineering, Al Akhawayn University, Ifrane, 53000, Morocco

Email: Oumayma Haberchad (o.haberchad@aui.ma) , Yassine Salih-Alj (y.salihalj@aui.ma)

*Corresponding author: Oumayma Haberchad, Dhahran, Saudi Arabia, +966537242208 & g202423940@kfupm.edu.sa

ABSTRACT: Real-time monitoring of injection molding parameters plays a pivotal role in enhancing product quality, reducing defects and improving production. This study presents a cavity data acquisition system for real time monitoring of process parameters inside the mold. The system consists of non-destructive in-mold sensors that monitor the status of the melt within the cavities. Furthermore, the geometry of the injected part is taken into consideration when selecting the position of the sensors. This enables early discovery of defects by studying abnormal variations of the monitored parameters in areas where these defects are suspected. A case scenario is shown in which we simulate the molding profile of a plastic part using SolidWorks Plastics. The suggested sensors' placements are then derived. Results indicate that the piezoelectric sensor measures with a root mean square error (RMSE) that is less than 0.0004 V and a peak error of 0.0012 V. The proposed method promises more control over injection conditions inside the mold, as well as enhanced overall production quality.

KEYWORDS: Injection Molding, Sensors, Data Acquisition, Process Monitoring; Quality Control.

1. Introduction

Since the invention of polymers, plastic products have been widely employed to meet basic demands and to replace expensive materials while providing competitive performance. Plastic's high popularity stems from its adaptability and capacity to mimic the functions of other materials while offering enhanced features such as corrosion resistance, low weight, flexibility, inexpensive production and maintenance costs [1].

Plastic manufacturing has significantly been used in many industries. The use of plastic in the automobile and aircraft industries led to a reduction in fuel consumption thanks to its light weight. Its usage in the medical industry improved safety and reduced contamination caused by metal equipment [2].

Different processes are used to produce plastic parts. This includes extrusion, thermoforming, blow molding, and injection molding.

Injection molding is a popular manufacturing technology. It is widely used in various industries, including automotive, medical, and electronics. The injection molding market have reached 305 billion USD in 2022 only, accounting for over one-third of total plastic manufacturing [3]. The sector has evolved significantly in recent decades. Concerns over plastic waste and Industry 4.0's demand for digitalized processes, including cyber-physical systems, are driving these changes [4]. To address these challenges, different methods have been proposed to automate and optimize the injection molding process [5], [6].

To fully regulate the injection molding process, machine and in-mold parameters, as well as part quality, must be monitored [7]. Tracking machine parameters offers real-time insight into the polymer's behavior during dehumidification, melting, and injection phases. Previous works have analyzed data from the injection machine to determine which parameters have the greatest impact on the quality of ejected parts [8]. This strategy produced notable outcomes. However, injection molding's non-iterative nature led to varying results across multiple manufacturing cycles.

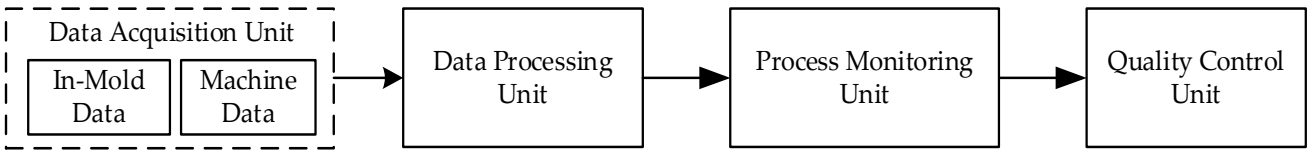

Figure 1: Block diagram of the considered cavity data acquisition system.

In mold process monitoring entails tracking the polymer melt (resin) during injection, cooling, and ejection. Previous works in the literature suggest that extracting data from a mold can provide better insights about melt status and behavior [7], [9].

Melt enters mold cavities later in the molding cycle. This stage involves sophisticated procedures including cooling, ejection, and most importantly, part formation. The polymer's condition can be closely monitored as it transitions from liquid to solid using in-mold sensors. While sensors have been used in machines since the 1960s, cavity sensors represent a recent technological adoption (10-12 years) [10]. This is due to the complex mounting of these sensors inside the mold which delays their mass integration.

However, with an increasing migration towards automated monitoring of industrial processes, cavity sensing technology has gained more popularity, and an array of new sensors has been developed to ensure agile integration into machinery.

Cavity sensors typically use piezoelectric and strain gauges for pressure measurement and thermocouples to monitor temperature [11]. These are available in various sizes and mounting options, allowing for full customization to meet quality standards. However, numerous limitations have been affecting their performance. For instance, sensors mounted in molds can be damaged by high pressure and temperature changes, leading to corrosion and frozen layers. This results in measuring inaccuracies. Additionally, while direct contact with the melt can result in accurate measurements, it may also cause surface level defects in the final product.

Thin-film sensors have also been investigated. They are made of piezoelectric sensors that are deposited into the steel surface via sputtering, allowing for precise pressure monitoring in various parts of the mold [7]. Temperature changes, however, significantly disrupt the signals affecting measurement accuracy.

Other alternative sensors have been proposed, including wireless piezoelectric sensors [12], infrared sensors [13], and optical sensors [14]. Although they are still in their early stages of implementation in industry, they provide efficient and precise measurements without direct contact with the melt which expands the range of parameters that can be monitored.

To allow full integration of cavity sensors with the other components of the mold, different Data acquisition systems have been developed. This includes an Arduino microcontroller-based data acquisition module that allows the visualization of different mold parameters including mold temperature, cavity pressure, 3-axis acceleration, and extraction force [15]. These were measured based on commercially available sensors including thermocouples, pressure sensors, and force sensors. The developed system allowed affordable, simple, and real-time data acquisition and monitoring of process parameters. Additionally, the system was able to distinguish between normal and abnormal patterns in monitored parameters. Although process variations were successfully captured, the wired nature of sensors used can cause potential hazards due to mold's movements. To overcome this issue, a multiple measurement sensor was adopted in [16] to measure temperature and pressure simultaneously. The sensor was equipped with a piezoelectric transducer for pressure measurement, and a K thermocouple for temperature measurement. This reduced the amount of holes required to insert sensors inside the cavities thereby minimizing structural damage to the mold. Other commercially available controllers include Priamus' Fillcontrol, BlueLine Hardware and QFlow Systems Engineering.

Considering cavity sensors' high efficiency in monitoring injection molding processes and addressing the lack of sufficient work recognizing the geometry of the part when selecting sensors, this work presents a data acquisition system for in-mold process control and monitoring. The system allows the measurement of injection molding process parameters inside the mold using cavity sensors. The main objective of the study is to select sensors capable of accurately monitoring cavity process parameters in areas where defects are suspected while taking into account the geometry of the part and without inducing destructive alterations to the mold. To achieve this, ultrasonic based sensors were proposed. These sensors are positioned based on the part's molding profile to identify abnormal melt flow and reduce defects. Thank to their wireless transmission scheme, these sensor reduce the amount of wholes and wires inserted into the mold resulting in a more robust process monitoring. The proposed approach can promote sustainable injection molding by decreasing waste and adjusting to future changes in the manufacturing process.

The remainder of the paper is structured as follows. Section 2 describes the theoretical model for cavity data acquisition. Section 3 presents the proposed data acquisition system.

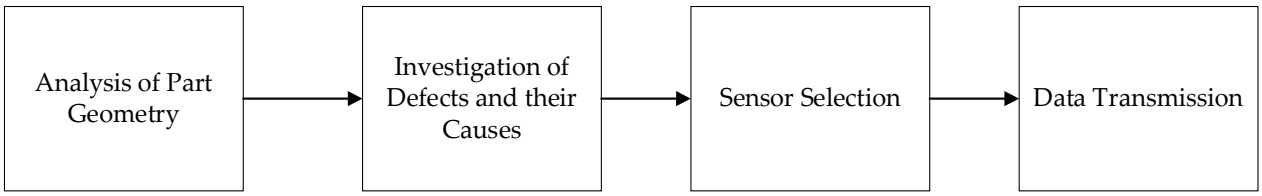

Figure 2 : System model of the data acquisition system.

Section 4 details the obtained simulation results. Finally, Section 5 concludes the paper.

2. Theoretical Model for Cavity Data Acquisition

This section presents the injection molding process cycle data flow. Figure 1 depicts four levels of data processing: data acquisition unit, data processing unit, process monitoring unit, and quality control unit [17].

2.1. Data Acquisition Unit

Data collection begins with measuring process parameters using sensors incorporated in both the injection machine and the mold. The machine is equipped with a complex set of sensors that allow for full monitoring of various process parameters such as maximum injection pressure, screw position, and temperature in different screw zones.

Due to direct contact with the melt, in-mold sensors are incredibly effective in describing melt flow behavior while being less complex. For instance, these sensors can measure mold temperature and pressure, melt flow, velocity, and viscosity [7].

2.2. Data Processing Unit

The data obtained from injection molding machines and in-mold sensors is then processed. The collected signals are amplified and filtered to remove noise and enhance the data. The continuous signals generated by the sensors are then sampled to improve computational efficiency and synchronize the numerous data sources.

2.3. Process Monitoring Unit

At this stage, the processed datasets are utilized to monitor injection cycles. Machine and mold parameters are visualized via graphical interfaces, allowing operators to track variations in process parameters as well as melt rheology to ensure that no disruptions influence production [6].

2.4. Quality Control

Once the part is ejected out of the mold, it undergoes multiple control procedures. First, when the injection cycle ends, and later once the visual and dimensional features of the part stabilize. This ensures that the part meets the standards set by the customer.

3. Proposed Data Acquisition System

In this section a detailed description of the proposed data acquisition system is given. As illustrated in Figure 2, four steps are to be implemented to develop the model: analysis of part geometry, investigation of defects and their causes, sensor selection, and data transmission.

3.1. Analysis of Part Geometry using CAD Software

Part design is the first step in the mold creation process. Computer-aided design simulations, such as Autodesk, Ansys, and SolidWorks, have made part design more automated. Injection molding software can design parts and simulate melt behavior. This provides valuable insights into how parameters vary during the filling process. Additionally, it allows for early detection of defects during the injection process.

3.2. Analysis of Defects and Their Causes

After the part is manufactured, the next step in implementing the suggested cavity data acquisition system is to analyze the injection molding defects associated with the mold. Weld lines, shrinkage, warpage, and sink marks are some of the most prevalent defects.

3.2.1. Weld Lines

Weld lines are plastic flow traces that resemble the letters J or U. This defect occurs when two fronts flow from different directions meet, resulting in weak regions in the component [18].

3.2.2. Shrinkage

Shrinkage is the reduction in volume caused by polymer cooling. Inconsistent contraction due to temperature variations in the various regions of the part causes shrinkage [19]. Despite its common occurrence, excessive shrinkage can cause geometric errors in plastic parts.

The shrinkage can be expressed using equation (1), [20]:

$$s_i = \frac{d_i - d_{si}}{d_i}, \tag{1}$$

where s is the shrinkage, d is the cavity width, and d_s is the part's width. The i subscript indicates the sensor's position. Using different sensors, temperature and pressure can be measured locally to calculate the overall shrinkage of the part.

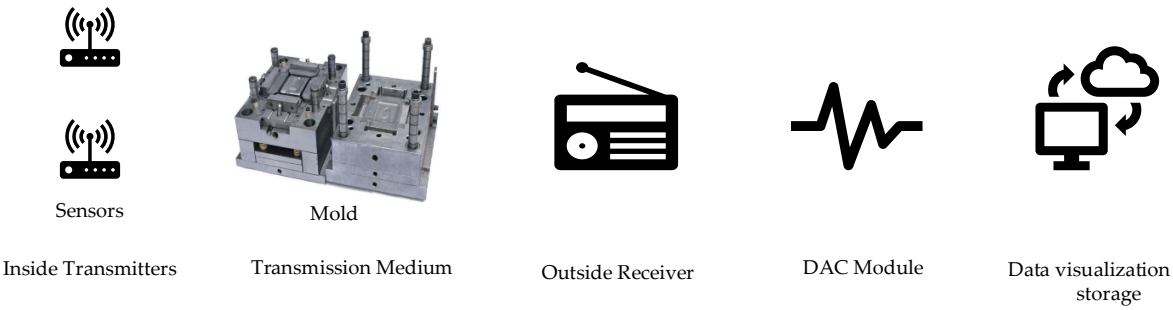

Figure 3 : Transmission scheme of data extracted from cavity sensors.

3.2.3. *Warpage*

Warpage occurs when internal forces cause a part to bend and deviate from its original geometry. Warpage, as is shrinkage, is induced by uneven part contraction and ongoing cooling after ejection, which causes parts with slower cooling rates to bend [19].

3.2.4. *Sink Marks*

Sink marks appear on surfaces with substantial wall thickness on the opposite side [18]. Such defects could occur due to fluctuations in cavity temperature, in addition to variations in other process factors including cooling time and packing pressure [21].

3.3. *Sensor Selection*

Mold sensors monitor numerous parameters inside the cavity, including pressure and temperature. This work considers sensors that take into account both defects and part geometry. To avoid damaging the mold during installation, two sensors are proposed: a wireless piezoelectric sensor and an ultrasonic sensor.

3.3.1. *Wireless Piezoelectric Sensors*

These sensors monitor pressure by transmitting energy from melt pressure, which also powers them [12]. An energy converter converts mechanical energy from the melt into electrical energy. The energy converted is expressed as follows:

$$E = \frac{1}{2} C \left(\frac{n \cdot d_{33} \cdot P \cdot A_{fp}}{C} \right)^2, \quad (2)$$

where C is the total capacitance, d_{33} is the charge constant, P is the pressure acting on the piezoceramic ring, A_{fp} is the footprint area where the pressure is acting, and n is the number of piezoceramic rings. For instance, electric charge is generated under mechanical stress induced by melt pressure. The resulting charge can be expressed as the product of the pressure acting on the ring, the footprint area over which the pressure is acting, and the charge constant. The electrical behavior of the piezoelectric rings can be approximated as a parallel plate capacitor. The ratio of the charge over the total capacitance of the system models the voltage generated, and it is related to the square root of the energy as expressed in equation 2.

The resulting electrical energy is discretized into electrical pulses using a threshold modulator. A signal transmitter converts the pulses into ultrasonic waves, which are subsequently delivered to a receiving unit outside the cavity.

3.3.2. *Ultrasonic Sensors*

Ultrasonic sensors are non-destructive and can measure parameters including melt homogeneity, temperature, and thickness [7]. Ultrasonic transducers use the converse piezoelectric effect to propagate ultrasonic waves [22]. Equations (2), (3), and (4) indicate how longitudinal ultrasonic velocity can be related to pressure and temperature using specific volume [23].

$$c_L = \left(\frac{1}{\rho \kappa} \right)^{\frac{1}{2}}, \quad (3)$$

where c_L is the longitudinal ultrasonic velocity, ρ is the density of the polymer melt, and κ is the adiabatic compressibility expressed as:

$$\kappa = -\frac{1}{v} \left[\left(\frac{\partial v}{\partial P} \right)_T + \frac{T}{c_P} \left(\frac{\partial v}{\partial P} \right)_P^2 \right], \quad (4)$$

where P is the melt pressure, T is the melt temperature, cp is the specific heat capacity, and v is the specific volume described by the Tait equation as [23]:

$$v(\mathrm{T}, \mathrm{P}) = v_0(T) \left[1 - C \cdot ln \left(1 + \frac{P}{B(T)} \right) \right] + v_t(T, P), \quad (5)$$

where v_0 is the zero pressure isotherms, $B(T)$ is a temperature dependent function, and C= 0.0894 is a universal constant [24].

As the melt temperature increases, the sound velocity decreases in an approximately linear manner. On the other hand, increased melt pressure drives sound velocity to higher levels.

3.4. *Data Transmission*

Given the sensors used, the data acquisition scheme is based on the transmission of ultrasonic waves, allowing wireless communication between the transmitter and receiver [25]. To illustrate, when cavity parameters are

monitored, they are transformed into a voltage, which is then discretized into pulses using a threshold modulator [12]. The pulsing voltage causes the piezoelectric material to be displaced, resulting in ultrasonic waves [22]. These waves can travel through the mold's walls. Then they are received by an external receiver, which turns them back into voltage. The cavity measurements are recovered by multiplying the number of received ultrasonic pulses by the modulator's threshold. To display and save the measurements, a data acquisition module (DAC) can be employed to transform the analogue signal to a digital one. Figure 3 shows the overall transmission scheme.

4. Simulation Results

4.1. Simulation Setup

To visualize the proposed system's mechanisms, a computer-aided engineering (CAE) simulation has been constructed in SolidWorks Plastic. We began by designing the part, as shown in Figure 4. The part investigated was designed to cause the previously mentioned defects.

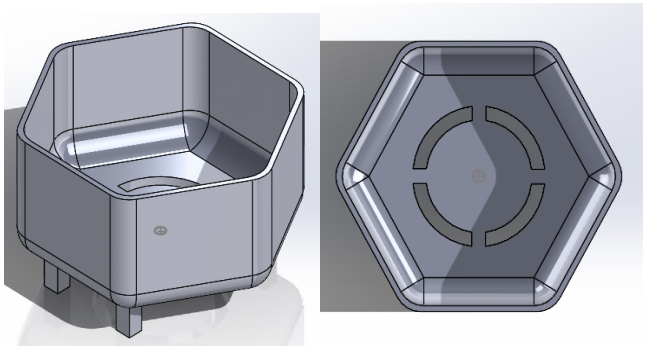

Figure 4 : CAD design of the studied part.

Then we proceed with the plastic flow analysis. The latter begins by defining the materials used. The chosen polymer is Acrylonitrile Butadiene Styrene (ABS), and its parameters are described in the SolidWorks plastic database, as seen in Table 1. This is followed by defining process parameters values for the simulation as expressed in Table 2. After that, the injection gate (through which the melt enters the cavity) was placed in the center of the part as seen in Figure 5.

Table 1: Material properties of ABS.

Property	Value
Melt Flow rate	35 g/10min
Max shear rate	50000 1/s
Max shear stress	0.3 MPa
Poisson's Ratio	0.39
Elastic Modulus	2250
Melt Temperature	230 °C
Max. Melt Temperature	280 °C
Min. Melt Temperature	200 °C
Mold Temperature	50 °C
Ejection Temperature	90 °C

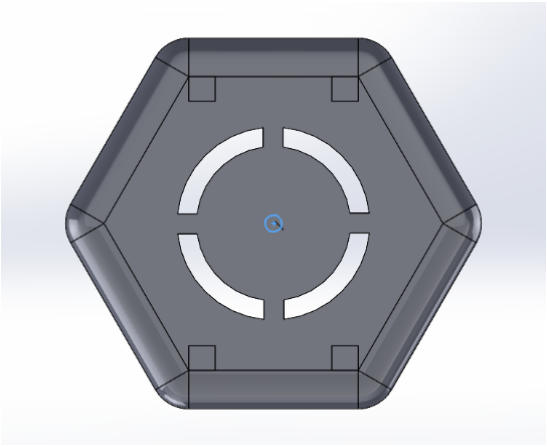

Figure 5 : Injection gate location.

Furthermore, a solid mesh with a total of 17410 triangular components measuring 5.19 mm was created as illustrated in Figure 6.

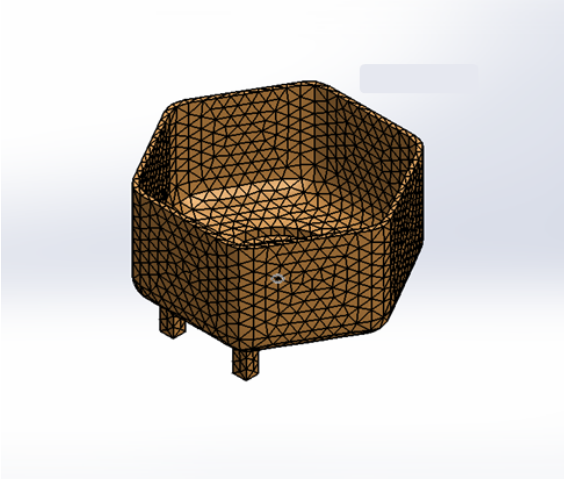

Figure 6 : Illustration of meshed part.

The simulation is then run, and the distribution of the various parameters and defects are shown.

Table 2: Simulation process parameter values.

Process parameter	Value
Melt temperature	230 °C
Mold temperature	50 °C
Injection pressure limit	100 MPa
Pure cooling time	31.163 s

4.2. Parameter Visualization

This section visualizes the various variables that control the process. The data was acquired after

performing the plastic flow simulation in SolidWorks Plastics.

In Figure 7, the max inlet pressure is visualized. We notice that the pressure increases until it reaches a maximum value of 13.488 MPa and then it decreases.

In Figure 8, the melt front flow rate versus time is visualized. We notice that the melted front flow rate varies increasingly until reaching a maximum value of 21.883 cc/s.

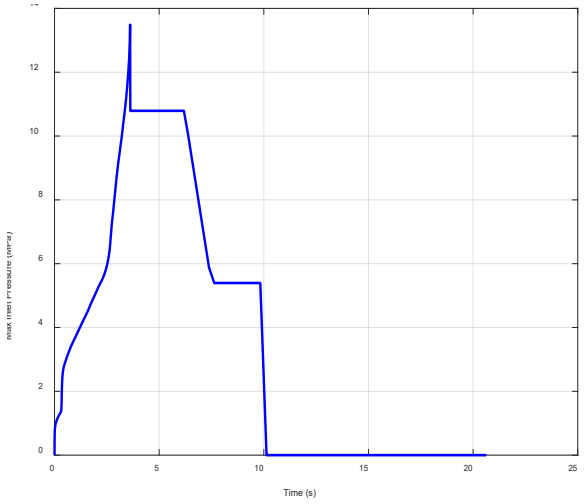

Figure 7 : Max inlet pressure versus time.

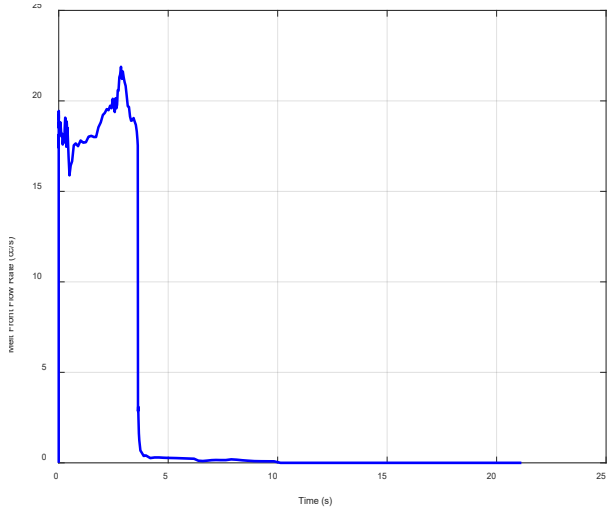

Figure 8 : Melt front flow rate versus time.

4.3. Analysis of Defects

In addition to analyzing the distribution of parameters within the cavity, fill and warp analysis enable us to identify potential defects that may appear during the molding process. The previously reported defects had been identified within the part after the simulations were completed.

Figure 9 depicts the distribution of sink marks in the portion. We notice that these marks are located in the lower area of the part because it has a high wall thickness, as well as in the four extruded pieces bearing the part, which have a high thickness and generate a depression on the other side of the part.

Figure 10 demonstrates the distribution of volumetric shrinkage. We observe that both the upper part and the gate endure significant shrinkage.

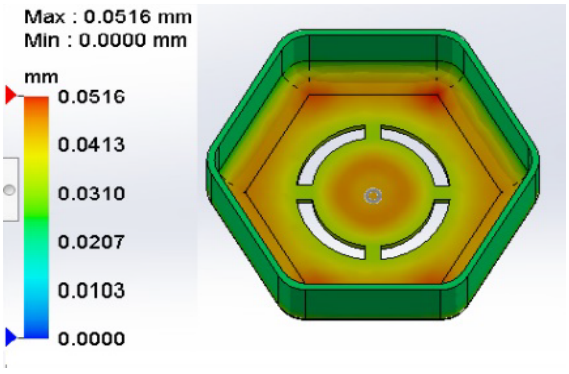

Figure 9 : Distribution of sink marks.

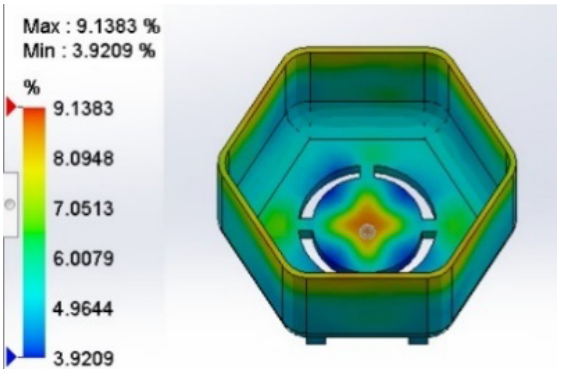

Figure 10 : Distribution of the volumetric shrinkage.

Figure 11 depicts the distribution of weld lines throughout the part. We notice that the weld lines are placed near the holes in the part, indicating that two melt flow fronts intersect in those areas.

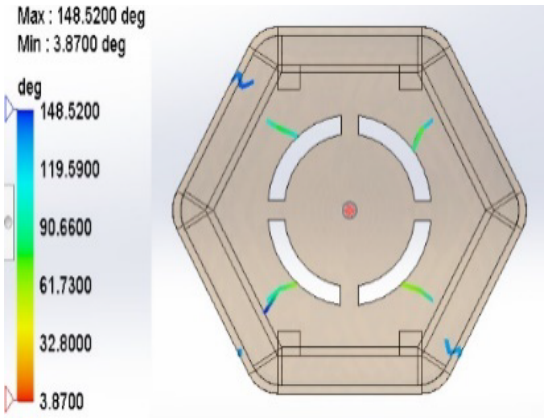

Figure 11 : Distribution of weld lines.

Figure 12 depicts the distribution of the total displacement of the part. The walls experience moderate warp levels, while the lower area experience greater warp.

4.4. Sensor's Placement

The system requires a total of five sensors, as shown in Figure 13. One wireless piezoelectric sensor will be installed where a sink mark is suspected in order to monitor pressure changes. Three more wireless piezoelectric sensors are utilized to monitor the part's shrinkage and displacement: one in the part wall, one at the top, and one at the bottom. One ultrasonic transducer

is used to measure temperature in the area where weld lines may appear.

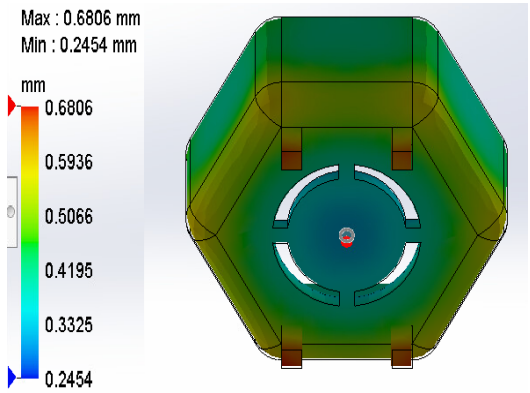

Figure 12 : Total stress displacement.

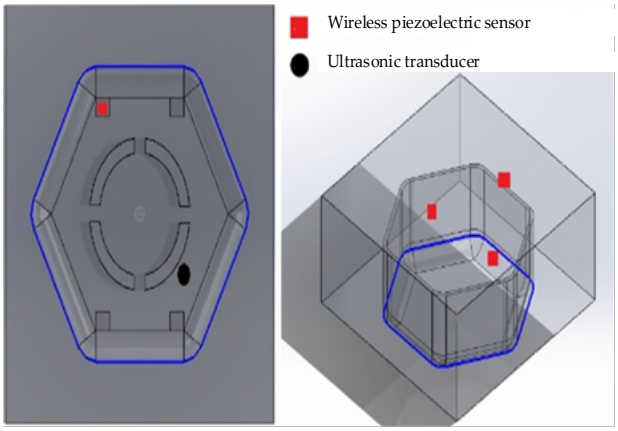

Figure 13 : Placement of the sensors inside the cavity.

4.5. Piezoelectric Sensor Measurement

Using data from the CAE simulation, we evaluate the signal transmitted by the piezoelectric sensor, Figure 14 illustrates the MATLAB block diagram. The input is the pressure of the area where sink marks are monitored. This pressure is transformed into a voltage [12]. Then noise is added to emulate real-world measurement disturbances from industrial environment.

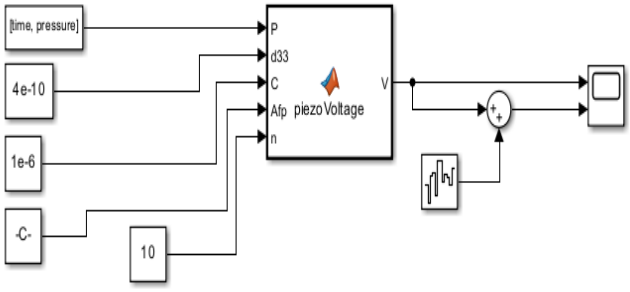

Figure 14 : Block diagram of piezoelectric sensor measurement.

Figure 15 illustrates the actual voltage while Figure 16 illustrates the measured one. We notice that the measured voltage depicts the variations of the actual voltage. By calculating the root mean square error (RMSE) and the peak error we found values of 0.0003 V and 0.0012 V respectively. This indicates that the proposed sensor accurately depicts the variations of pressure in the specified region, allowing early detection of the appearance of sink marks.

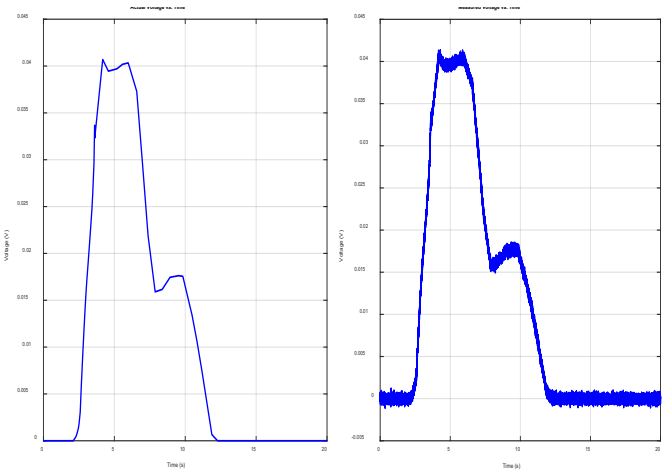

Figure 15 : Graph of the actual voltage and the measured voltage.

5. Cost Study

To assess the system's profitability and its potential impact on plastic part manufacturing, we propose a cost analysis based on a large production volume injection molding process [26]. The production cost of the part and the system's implementation expenses are shown in Table 3. Production volume, production technique, mold type and cost, lead time to final component, material cost, labor cost, and outsourcing cost are all factors that go into estimating the product's cost. Fixed costs on the other hand cover the data acquisition system's initial deployment fees.

Table 3: Detailed costs.

Variable Costs	Amount (USD)
Part cost	1.70
Production volume per month	100,000.00
Total	170,000.00
Fixed cost	
Sensor price	750.00
DAC module	108.00
Overhead costs	4,000.00
Selling expenses	1,000.00
Investment costs	5,000.00
Management expenses	2,000.00
total	12,858.00
Sales	
Part price	4.00
Total	400,000.00

To measure the effect of the system on production we implemented a breakeven analysis as seen in Figure 16. The break-even point is calculated using the following equation (5):

$$Breakeven\ point = \frac{fixed\ cost}{selling\ price\ per\ unit - variable\ cost\ per\ unit}, \quad (6)$$

The breakeven point for the suggested system was 5,590 units. Considering a monthly production and sales volume of 100,000 units, the system's implementation expenses will be recovered within the first month of adoption.

It is also important to mention that the acceptable percentage of scrab can vary between 1% to 5%. If we consider a monthly plastic production of 100,000 parts weighing 20 g, the total amount of plastic waste generated monthly will be between 20 kg to 100 kg. These values are very high considering that the cost of raw material ranges from $1 to $5 per kilogram, and the high carbon footprint of ABS estimated at 146 g CO2e/kg [27]. Therefore, successful implementation of the system will lead to a reduction of scrab, and pollution generated by injection molding.

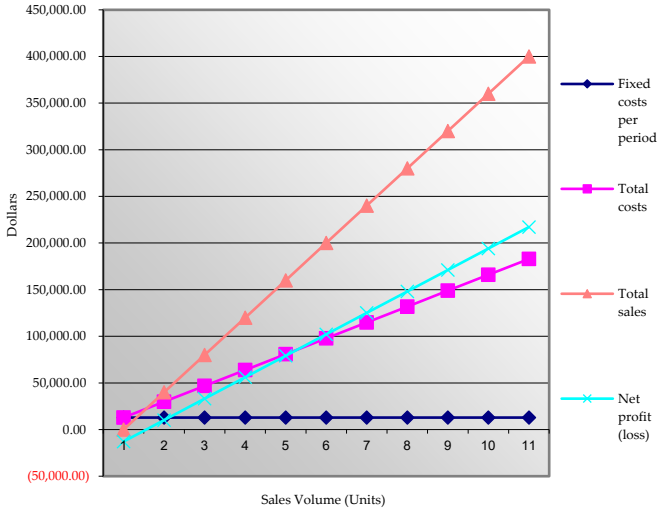

Figure 16 : Breakeven analysis chart.

6. Conclusion

In this paper, a cavity data acquisition system for in-mold process monitoring was proposed. The system allowed non-destructive measurement of cavity process parameters thanks to the use of piezoelectric and ultrasonic sensors.

The system has been developed in various phases, starting with part analysis using CAD software, followed by an investigation of defects and their causes, the sensors selected have then been described, and finally, the transmission scheme has been detailed.

Simulation results illustrated that CAD software can simulate melt behavior while allowing early detection of abnormalities and planning of sensor positioning. Similarly, piezoelectric sensors demonstrated accurate measurement of pressure showcasing that ultrasonic-based transmission of data is the best method for nondestructive monitoring of injection parameters within the cavity.

A draft cost analysis has been proposed to illustrate the cost effectiveness of the system and the short recovery of investment costs.

These results highlight the ability of the system to control injection conditions inside the mold while also improving production quality and reducing injection molding costs.

Although virtual testing provided an efficient evaluation of the system, on-site testing would allow practical investigation and examination of how the dynamic nature of the process may affect the system's capabilities. Additionally, the performance of the proposed sensors can be compared to emerging sensors such as infrared and to other commercially available sensors. Furthermore, the proposed system can be evaluated on other plastic parts to test its reliability on injection systems with varying degrees of complexity.

Future work would address the highlighted limitations and investigate the integration of a real-time control system to allow automated adjustment of in-mold parameters.

Conflict of Interest

The authors declare no conflict of interest.

References

[1] B. P. Federation, "Plastics applications," British Plastics Federation. [Online]. Available: https://www.bpf.co.uk/plastipedia/applications/Default.aspx

[2] M. Naik, "5 ways plastics revolutionized the healthcare industry," MPO Magazine, Oct. 09, 2017. [Online]. Available: https://www.mpo-mag.com/exclusives/5-ways-plastics-revolutionized-the-healthcare-industry/

[3] K. Pulidindi and K. Ahuja, "Injection molded plastics market size, growth report – 2032," Global Market Insights Inc. [Online]. Available: https://www.gminsights.com/industry-analysis/injection-molded-plastic-market

[4] G. Berger-Weber and S. S. Aminabadi, "The injection mold as a cyber physical system: Using simulation to train its artificial intelligence," in Proc. 29th Leoben Kunststoffkolloquium, Leoben, Austria, vol. 29, pp. 1–10, Sep. 2021.

[5] J. Krantz et al., "In-mold rheology and automated process control for injection molding of recycled polypropylene," Polym. Eng. Sci., vol. 64, no. 9, pp. 4112–4127, Jun. 2024, doi: 10.1002/pen.26836.

[6] M. Baum, D. Anders, and T. Reinicke, "Enhancing injection molding simulation accuracy: A comparative evaluation of rheological model performance," Appl. Sci., vol. 14, no. 18, p. 8468, Sep. 2024, doi: 10.3390/app14188468.

[7] T. Ageyeva, S. Horváth, and J. Kovács, "In-mold sensors for injection molding: On the way to Industry 4.0," Sensors, vol. 19, no. 16, pp. 1–21, Aug. 2019, doi: 10.3390/s19163551.

[8] B. Silva, J. Sousa, and G. Alenya, "Machine learning methods for quality prediction in thermoplastics injection molding," in Proc. Int. Conf. Electr., Comput. Energy Technol. (ICECET), Cape Town, South Africa, pp. 1–6, Dec. 2021, doi: 10.1109/ICECET52533.2021.9698455.

[9] G. Gordon, D. O. Kazmer, X. Tang, Z. Fan, and R. X. Gao, "Quality control using a multivariate injection molding sensor," Int. J. Adv.

Manuf. Technol., vol. 78, no. 9–12, pp. 1381–1391, Jan. 2015, doi: 10.1007/s00170-014-6706-6.

[10] V. Vara, "The benefit of pressure sensor in injection moulding," Efficient Innovations. [Online]. Available: https://www.efficientinnovations.in/the-benefit-of-pressure-sensor-in-injection-moulding/

[11] A. Schott et al., "Development of thin-film sensors for in-process measurement during injection molding," Procedia CIRP, vol. 120, pp. 619–624, Jan. 2023, doi: 10.1016/j.procir.2023.09.048.

[12] L. Zhang et al., "A self-energized sensor for wireless injection mold cavity pressure measurement: Design and evaluation," J. Dyn. Syst. Meas. Control, vol. 126, no. 2, pp. 309–318, Jun. 2004, doi: 10.1115/1.1767850.

[13] A. S. Babalola, "Design and construction of a sensor analytic system for the monitoring of the parameters of a plastic injection mould," Front. Eng. Built Environ., vol. 1, no. 1, pp. 32–40, May 2021, doi: 10.1108/FEBE-02-2021-0003.

[14] A. Bur and C. Thomas, "An optical sensor for polymer injection molding," Electrochem. Soc. Trans., 2000. [Online]. Available: https://tsapps.nist.gov/publication/get_pdf.cfm?pub_id=851715

[15] T. E. P. Gomes et al., "Development of an Open-Source Injection Mold Monitoring System," Sensors, vol. 23, no. 7, p. 3569, Mar. 2023, doi: 10.3390/s23073569.

[16] R. M. C. Bernardo et al., "Instrumentation and In-mould Data Acquisition System for Injection Moulding Process," 2023 4th Int. Conf. Artif. Intell., Robot. Control (AIRC), Cairo, Egypt, 2023, pp. 53–57, doi: 10.1109/AIRC57904.2023.10303047.

[17] O. Haberchad and Y. Salih-Alj, "A cavity data acquisition system for defect prevention in injection molding," in Proc. 10th Int. Conf. Appl. Syst. Innov. (ICASI), Kyoto, Japan, pp. 244–246, 2024, doi: 10.1109/ICASI60819.2024.10547795.

[18] B. Olmsted and M. Davis, *Practical Injection Molding*, 1st ed. Boca Raton, FL, USA: CRC Press, 2001, pp. 1–232, doi: 10.1201/9781482294590.

[19] N. Zhao et al., "Recent progress in minimizing the warpage and shrinkage deformations by the optimization of process parameters in plastic injection molding: A review," Int. J. Adv. Manuf. Technol., vol. 120, no. 1–2, pp. 85–101, Feb. 2022, doi: 10.1007/s00170-022-08859-0.

[20] S. Jiang et al., "Reducing the sink marks of a crystalline polymer using external gas-assisted injection molding," Adv. Polym. Technol., vol. 2020, pp. 1–8, Feb. 2020, doi: 10.1155/2020/3793505.

[21] M. Kariminejad et al., "Ultrasound sensors for process monitoring in injection moulding," Sensors, vol. 21, no. 15, pp. 1–22, Jul. 2021, doi: 10.3390/s21155193.

[22] V. Speranza, U. Vietri, and R. Pantani, "Monitoring of injection moulding of thermoplastics: Adopting pressure transducers to estimate the solidification history and the shrinkage of moulded parts," Strojniški Vestn. – J. Mech. Eng., vol. 59, no. 11, pp. 677–682, Jul. 2013, doi: 10.5545/sv-jme.2013.1000.

[23] K. Straka et al., "To the measurement and influences of process parameters variations on the axial melt temperature profile in the screw chamber of an injection molding machine," in Proc. SPE ANTEC, Anaheim, CA, USA, pp. 1645–1651, May 2017.

[24] B. Praher et al., "Ultrasound based monitoring of the injection moulding process: Methods, applications and limitations," AIP Conf. Proc., pp. 159–162, Jan. 2014, doi: 10.1063/1.4873755.

[25] Y. Li et al., "An optimal design method for improving the efficiency of ultrasonic wireless power transmission during communication," Sensors, vol. 22, no. 3, p. 727, Jan. 2022, doi: 10.3390/s22030727.

[26] "How to estimate injection molding cost?," Formlabs. [Online]. Available: https://formlabs.com/global/blog/injection-molding-cost/

[27] J. Tinz, T. De Ancos, and H. Rohn, "Carbon Footprint of Mechanical Recycling of Post-Industrial Plastic Waste: Study of ABS, PA66GF30, PC and POM Regrinds," Waste, vol. 1, no. 1, pp. 127–139, Dec. 2022, doi: 10.3390/waste1010010.

OUMAYMA HABERCHAD received a bachelor's degree in general engineering with a concentration in mechatronics at Al Akhawayn University in Ifrane (AUI). She is pursuing her Ph.D. at King Fahd University of Petroleum and Minerals in Systems and Control Engineering. She served as a research assistant in the Interdisciplinary research center for smart mobility and as a data analyst at the office of institutional research and effectiveness. She participated in fieldwork experiments to collect data on risk-taking in rural areas. She served in the automotive industry as a product engineer. She has published five papers. Her research interests include sustainable manufacturing, robotization, digitalization, data analysis, and geographic information systems.

YASSINE SALIH ALJ received the Bachelor's degree in microelectronics from the University of Quebec at Montreal (UQAM), Montreal, Quebec, Canada, in 2001, and the Master's degree in electrical engineering from the École de Technologie Supérieure (ETS), Montreal, Quebec, Canada, in 2003, and the Ph.D. degree in Telecommunications from the National Institute of Scientific Research – Energy, Materials & Telecommunications (INRS-Telecom), Montreal, Quebec, Canada, in 2008. He served as a research assistant at the Telebec Underground Communications Research Laboratory (LRTCS) from 2005 to 2008, and then during 2009 as a Postdoctoral Fellow at Poly-Grames Research Center, of the École Polytechnique de Montréal, Montreal, Quebec, Canada. He is currently working as a Full Professor of Engineering at the School of Science and Engineering (SSE) of Al Akhawayn University in Ifrane (AUI), Morocco, where he also served during 2019-2022 as Academic Coordinator for General Engineering programs (GE and RESE majors - Renewable Energy Systems Engineering). He has published over 80 publications and has been actively involved in IEEE events for the past five years, where he chaired and served as Technical Program Member or as distinguished

reviewer for over 200 conferences. His research interests are in the areas of Wireless Communications, Indoor Positioning, UWB (Ultra-Wideband), Smart Systems, GPS (Global Positioning System) and Engineering Education.

JENRS

Received: 18 April, 2025, Revised: 22 May, 2025, Accepted: 23 May, 2025, Online: 28 May, 2025

DOI: https://doi.org/10.55708/js0405003

Electric Transmission from Sarawak to Singapore Using Cable Suspended within O&G Pipes

Prashobh Karunakaran*, Mohd Shahril Oaman [1], Salim Sulaiman Maaji [1], Chee Cheng Sung [2]

[1] SET, CRISD, University of Technology Sarawak (UTS), Sibu, 96000, Malaysia

[2] School of Computer Science, University of Nottingham, NG8 1BB, United Kingdom

*Corresponding author: Prashobh Karunakaran, 19 Greenwood Park Phase 4, 93250 Kuching, Malaysia, 6-0128879578, prashobh.karunakaran@gmail.com

ABSTRACT: Running HV cables within pipes has been done since the 1970s but not fully utilizing the piping expertise developed by the O&G industry since 1859. The O&G industry has laid pipes on the seabed over a vast area north of Sarawak. This research studies the feasibility of utilizing this available industry to send power from Sarawak to Singapore. A HV cable will be suspended at the center of O&G pipes pumped with air at 7 atm. Another pipe will return the air back to Sarawak to be cooled and recycled. This will simulate the higher power transmission capability of overhead lines compared to submarine cables. The media is currently broadcasting that a submarine cable will send power from Sarawak to Singapore. But without thermal dissipation for the Joule heating generated over the 700 km cable, there will be reduced efficiency and a higher probability of failure. The lab experiment done was to send 0 - 50A, in steps of 5A, in a cable suspended at the center of pipes of varying Ø. The eddy current generated heat on the pipe was measured. This data is then extrapolated to forecast if 1000 A is sent in a Ø = 2m pipe.

KEYWORDS: Submarine transmission, XLPE, HDPE, steel, electric transmission within pipes, eddy current, Joule heating

1. Introduction

1.1. Current plan and associated challenges

The current plan which was broadcasted in the media is to send electricity from hydroelectricity power rich Sarawak to Singapore via a 700 km long HVDC (High Voltage Direct Current) XLPE (cross-linked polyethylene) insulated submarine cable.

But Table 1 indicates a significantly higher capability of bare overhead (O/H) lines in power transmission compared with XLPE insulated submarine cables.

The current longest XLPE submarine cable in the world today is between Norway and the Netherlands which is only 580 km and 700 MW. Comparatively the current longest O/H cable is 2,375 km, 7,100 MW, bare aluminum in Brazil between Madeira to Rio de Janeiro [1]. Therefore, the O/H line in Brazil is 409% longer than the XLPE insulated submarine cable in Norway

Table 1: A comparison of the transmission capability of HDPE covered cable versus bare O/H lines

Longest submarine cable	580 km, 450 kV, 700 MW XLPE HVDC cable between Norway and Netherlands
Longest bare O/H line	2,375 km, 600 kV, 7,100 MW bare overhead line between Rio Madeira HVDC system in Brazil.

$$\frac{2375}{580} X\ 100 = 409\% \text{ longer}$$

$$\frac{7100}{700} X\ 100 = 1014\% \text{ more power}$$

And the power carrying capacity of the O/H line in Brazil is 1014% higher than the submarine cable in Norway.

The figure mentioned in the media for the currently proposed XLPE insulated submarine cable is 6 billion USD while the O&G (Oil & Gas) piping contractor who was consulted in Bintulu, Sarawak estimated that the CIP (Cable in Pipe) system proposed in this research will cost MYR 1 billion (USD 213 million) which is 2,816% cheaper than the XLPE submarine cable method.

$$\frac{6000000000}{213000000} X\ 100 = 2{,}816\%$$

The reason for the low power carrying capacity of XLPE cables is that there is no vent for the heat generated as electrons encounter resistance in the cable because it is covered by a significant amount of XLPE insulation which traps heat within the cable. Electricity flow in a conductor is due to electron flow within the conductor and the greater longitudinal flow versus lateral flow, the lower the electrical resistance as well as heat generated. Higher insulation over the conductor causes higher lateral flow in the conductor which produces more heat and therefore eventually even more lateral flow. In superconductors the electron flow does not scatter, which explains its zero resistance.

Fig. 1 is an observation from the experiment described in the methodology of this paper. It can be noticed from the infrared image that the PVC insulated portion of the cable is white color which is the maximum heat measurable by the infrared camera as depicted in heat legend at the right of the image. The portion of the cable which is stripped of the PVC (therefore bare Cu) is green to yellow in color which is cool according to the legend. In this experiment, 63 A was sent in a bundle of 4 X 2.5 mm^2 cables. Each 2.5 mm^2 cable can carry 21 A, therefore 4 X 2.5 mm^2 can carry 21 X 4 = 84 A, but is carrying 63 A in this experiment. Wires will experience significant temperature increases due to Joule heating when the current it is carrying is close or above the current carrying capacity of the cable.

Another indicator that covering cable with a high dielectric strength material reduces the current carrying capacity is shown in Table 2 which is the table published by The Institution of Engineering and Technology (IET) and is used by wiremen to decide which cable to use in most Commonwealth countries. Three red circles are drawn on the three columns, the first of which is where two cables are in a conduit within thermal insulation meaning the conduits are buried in cement walls. The second red circle is on the column where the two cables are in a conduit fixed on a wall and the third red circle is on the column where the cable is directly clipped on the wall. The insulation surrounding the conductor is highest in the first of these columns, second highest in the second column and least in the third column. Therefore, it can be noted that the current carrying capacity is inversely proportional to the amount of insulation around the cable increasing from 11 A, 13.5 A to 15.5 A [2].

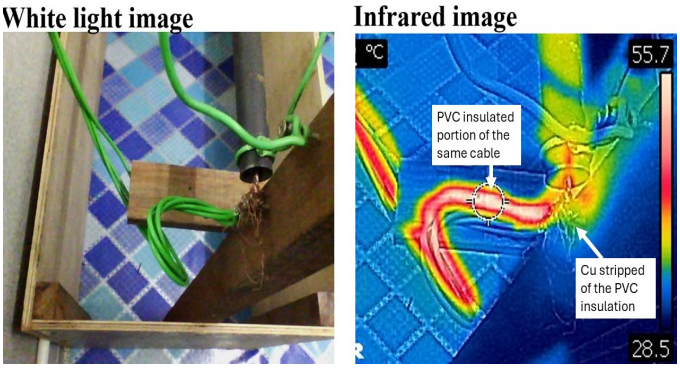

Figure 1: While conducting experiments, the above was noticed, the PVC insulated wire carrying 63 A was hot while the insulation stripped portion indicated is cool

Table 2: The IET table used in deciding which wireman use to determine wire size

Cross sectional area	In conduit in thermal insulation	In conduit in thermal insulation	In conduit on wall	In conduit on wall	Clipped direct	Clipped direct	Volt drop	Volt drop
mm^2	A	A	A	A	A	A	mV/A/m	mV/A/m
-	2 cables	3 or 4 cables	2 cables	3 or 4 cables	2 cables	3 or 4 cables	2 cables	3 or 4 cables
1.00	11.00	10.5	13.5	12	15.5	14	44	38
1.50	14.50	13.5	17.50	15.5	20	18	29	25
2.50	19.50	18	24	21	27	25	18	15
4.00	26.00	24	32	28	37	33	11	9.5
6.00	34	31	41	36	47	43	7.3	6.4
10.00	46	42	57	50	65	59	4.4	3.8
16.00	61	56	76	68	87	79	2.8	2.4

1.2. Brief description of solution worked upon in this work

It is possible to simulate O/H conditions under the sea following the schematic of Fig. 2. Each O&G pipe is 11.5 m. Binding wire can be used to fasten the conductor to the three insulators at the star point. Air at 7 atm can be pumped within the pipe and a second pipe will send the air back to Kuching to be cooled and recycled in the pipe with the conductor. This is a hypothesis, but it might be necessary to send the higher dielectric strength and less combustible N_2 within the pipe. The cheaper air (78% N_2) must be tried prior to using N_2. It must be noted that the highest pressure for gas in O&G pipes is 197.4 atm. Therefore if 7 atm does not provide sufficient dielectric strength, the pressure can be increased up to 197 atm.

The purpose of the robot in the figure is to enable human operators to view what is happening within the pipe via a camera. These robots will be energized by harvesting electromagnetic energy from the power line.

2. Literature review

According to Wong, J. (2025, February 28) article in the Borneo Post newspaper article, the proposed XLPE submarine cable between Sarawak and Singapore is carrying 1GW. This will require a 500 m^2 (0.0005 m^2) aluminum ($\varrho = 2.65\ X\ 10^{-8}$) at 1 GW (1000 A X 1000 kV):

$$P = VI \quad (1)$$

$$1\ GW = (1000\ kV)I$$

$$\frac{1\ X\ 10^9 W}{1\ X\ 10^6\ V} = I$$

$$I = 1000\ A$$

The resistance in a conductor follows equation (2) and the heat or Joule heating of the conductor follows equation (3).

$$R = \frac{\rho L}{A} \quad (2)$$

$$R = \frac{2.65\ X\ 10^{-8}\ X\ 700\ km\ X\ 1000\ m}{0.0005\ m^2}$$

$$R = 37.1\ \Omega$$

$$P_{loss} = I^2 R \quad (3)$$

$$P_{loss} = 1000^2 (37.1)$$

$$P_{loss} = 37{,}100\ watt$$

$$P_{loss} \approx 37\ kW\ (1kW = 1\ kJ\ per\ second)$$

Therefore, for every 1000 A sent to Singapore, 37 kilojoules per second will be lost, or 0.004% of the energy is emitted by the Al cable as heat every second.

$$\frac{37\ kJ}{1\ GJ}\ X\ 100\ \% = 3.7\ X\ 10^{-3} \approx 0.004\%$$

The problem is that at 1000 kV, the chance of dielectric breakdown through the XLPE is much higher. This means the thickness of the XLPE must be increased but when this thickness is increased, the heat is further trapped within the XLPE cable. Assuming the worst-case scenario of no heat escaping the XLPE covered cable, which is a reasonable assumption because at 1000 kV in the Al cable, that much plastic insulation is required to prevent arching to the 0 V sea water. With this assumption, the magnitude of heat trapped within the 700 km cable over a year will be:

$$37\frac{kj}{s}\ X\ 60\ \text{seconds}\ X\ 60\ minutes\ X\ 24\ hours\ X\ 365$$

$$Energy\ build\ up\ per\ year = 1.16\ X\ 10^{12}\ J$$

$$= 1160\ \frac{GJ}{year}$$

It must be noted that it takes 150 kJ/kg to melt XLPE and 390 kJ/kg to melt aluminum. Therefore, it is possible the cable may even melt if electricity is sent through it from Kuching to Singapore.

Another important factor comparing the Norway-Netherlands line to the planned Kuching-Singapore line is that Norway is one of the coldest countries on earth with an average ocean bed depth of 2000 m and temperatures of **1–2 °C** throughout winters and summers. Comparatively the Sunda Shelf as depicted in Fig. 3 between Kuching and Singapore is one of the shallowest seabed on earth with an average depth of 50 m and temperature of **23.6 °C**. The Sunda Shelf was created after an ancient global warming event that impounded the Sunda Shelf (1.85 million km² in surface area), which separated Borneo from the rest of Asia; this is why it is one of the shallowest seas on earth, with much of it being only 20 m deep [3].

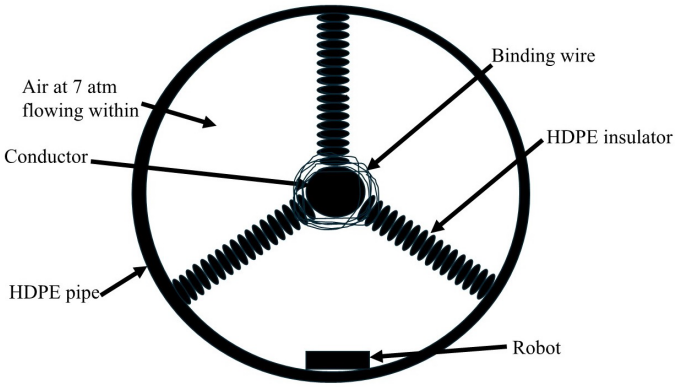

Figure 2: The proposed Cable in Pipe system

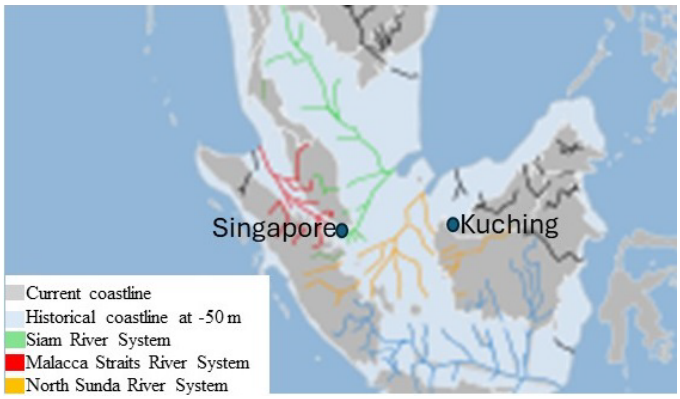

Figure 3: The Sunda Shelf with the location of Kuching and Singapore specified

All the above data listed so far in this paper indicates that it is better to simulate O/H line conditions for the power link between Kuching and Singapore. This can be achieved via suspending the bare conductors in O&G pipes as shown in Fig. 2.

One of the arguments for using the standard XLPE submarine cable is that large companies like Siemens are supporting it and if they build it, they must wager the reputation upon it. But the current cable builder is not from any of the largest electrical equipment suppliers on earth, which are GE Vernova, Siemens, ABB and Schneider.

Underground (U/G) cables are banned in Thailand. Therefore, the prevalence of overhead lines alongside dense telecommunication lines on poles are a notable characteristic of Thailand's utility infrastructure. But despite that ugliness, Thailand has the cheapest internet access in Southeast Asia (SEA).

One Telco technician informed this author that in Kuala Lumpur where it often floods in the tunnels they used to carry telecommuting fiber optic cables, electronic switches are frequently covered with water which damages them. Because of this, customers who were promised a certain GB of data transmission will get only a fraction of it. Such a scenario would not occur in Thailand with O/H lines. It is also much easier to maintain O/H lines.

Digging with excavators for underground cable repair often results in roads and pavements that are never fully restored to their original condition.

Another significant aspect of the proposed submarine cable from Sarawak to Singapore is its historical context: advertisements for the Bakun Dam, widely publicized in local papers since the 1970s, consistently featured a corresponding submarine cable. In 2009, this author inquired with a senior manager of the local electrical authority (LEA) about the fate of that line. He responded that the LEA's extensive research concluded significant power loss would occur by the time the line reached Johor which is about 1 km from Singapore (Peter Ngaim, personal communication, June 21, 2009).

A concern expressed about this CIP system is that there may be leaks of sea water into the pipe. But the O&G industry has long developed pipes to handle 7 atm of pressure of oil or gas. A leak of sea water into the pipe will cause an earth fault (E/F) and the protection system will trip the line from Sarawak to Singapore. The only consequence may be a tripping of power in Singapore which will not be considered a big issue by the 8.1 billion people on earth today. Other power stations in Singapore, Malaysia or Indonesia can easily back up the loss power in a short span of time.

Comparatively a leak of oil or gas out of an O&G pipe will cause international headlines in all news media and even a large company like Shell plc's stock market value will plummet as explained by a manager in Shell plc, [Karunakaran Praveen, personal communications, 26/1/2022]. Therefore, the risk of a leak is far greater for the O&G industry compared to the electric companies planning to send electricity from Kuching to Singapore.

This much lower tolerance for failure for the O&G industry has resulted in a long continual development of the integrity of O&G pipes, which can be trusted to a very high percent for the designed purpose in this research.

The Life Cycle Assessment (LCA) using the cradle-to-grave methodology of pumping the pipe with N_2 can be significantly high therefore it is better to try using 7 atm of air for a few km of CIP (Cable in Pipe) before expanding it to 700 km.

A CIP method of transmitting power is already commonly used in GIS (Gas Insulated Substation). Fig. 4 depicts the GIS substation in Bintulu, Malaysia. The cost is high probably because it was totally designed by the electric power industry and not utilizing the long expertise in the piping field of the O&G companies. GIL (Gas Insulated Lines) lines have been developed since the 1970s.

In AIS (Air Insulated Substation) the high voltage cables need a specific separation distance which is proportional to their voltage level. Therefore, in places like Tokyo or Hong Kong where land prices are extremely high, it is worth it to use GIS substations where GIL enables placing the HV (High Voltage) lines closer to each other, thereby saving cost of real estate. The pipes in GIL lines are pumped with a mixture of N_2 and SF_6.

Figure 4: GIS substation in Bintulu, Malaysia which uses GIL lines.

GIL lines, specifically manufactured by Siemens, are also used to send HV power down coal mines where the tunnels are not big enough to provide suitable separation distance between the HV phase lines and the humans. Similarly in hydroelectricity power stations, the turbines must be located very low since they are tapping the power of gravity. From the turbine, a shaft from it turns the generator rotor. But this shaft cannot be too long because it will break due to the torsional forces acting on it. But power from the generators must be sent to the top surface if AIS substations need to be used. Therefore, many hydroelectric power stations place the generator just above the turbine and use GIL lines to send power to the AIS substations located at the top of the dam. As for electricity transmission, the current longest GIL line is from Suzhou to Taizhou in China, which is 5.5 km at 1000 kV [4].

The oil and gas (O&G) industry has a long history of laying pipelines off the coast of Sarawak. During a visit to an O&G piping vendor's office in Miri, this author observed a large map of Sarawak's offshore area displaying detailed pipeline routes. The extensive network of pipes visually appeared to cover an area larger than Sarawak's landmass, underscoring the vastness of the subsea infrastructure. While the majority of these pipes are constructed from carbon steel, a small proportion are made of High-Density Polyethylene (HDPE). These pipelines commonly transport oil and gas at pressures in the tens of atmospheres (e.g., 10-100 atm) in shallow waters (less than 500 meters deep), with pressures in deepwater applications (over 1500 meters deep) potentially reaching hundreds of atmospheres, and in specialized cases (such as high-pressure well flowlines), even exceeding 800-1000 atmospheres (Soegiarto, Bennet, personal communications, 21/6/2023].

The Georgia Power company, USA provided the results of their study which is that U/G XLPE cables can cost eight times more than O/H lines, has a lifespan of half of O/H lines (35 years for U/G cables versus 80 years for O/H), repair time of 192 hours (> one week) compared to three hours for O/H lines. While their advantages are only beauty and ability to withstand typhoons better [5].

Other than being a university lecturer, this author is a lecturer of electrical engineering for electrical contractors. The government requires the contractors to attend such courses to get points to renew their contractor licenses. Once as he was teaching all the top electrical contractors in the second biggest city in Sarawak, Malaysia where he mentioned all the above results from Georgia Power company, USA. All the contractors agreed but the largest contractor company owner raised his hand to say that there is one advantage for U/G cables which is that he makes a lot of profit if he uses U/G cables. At eight times the price for U/G cables, 20% profit of 100 million is surely less than 20% profit of 800 million.

The Paschen Curves are commonly used to determine the relationship of pressure (in Torr) and the distance between electrodes for different gases [6]. Using SF_6 for the CIP project, as is currently widely used as a dielectric in the electric industry, is impractical because it has the highest global warming potential (GWP). SF_6 is also an infrared (IR) absorber. It is because of these facts that the electric industry is currently finding an alternative to SF_6 due to environmental concerns [7]. Studies have shown that the highest dielectric strength is achieved by a mixture of 60% SF_6 and 30% N_2 [8]. N_2 is an inert and environmentally friendly gas which comprises 78% of the current atmosphere. Between 1970 – 2000, GIL used 100% SF_6 as the dielectric. From 2000 – 2024 a mixture of SF_6 and N_2 has been used in GIL. Currently synthetic gases are being developed to be the dielectric for GIL because of the global warming potential of SF_6. SF_6 will only break up in the atmosphere after 3200 years compared to 650 years for CO_2 [9].

Table 3 shows the dielectric strength of various materials of interest to this topic. Distilled water seems to have a much higher dielectric strength than SF_6 and it is liquid which is easier to prevent leaks from pipes holding it but it has been proven in labs that when 50 kV is in the cable, even distilled water can electrolyze into H_2 and O_2 which is an explosive mixture near possible arcs in the pipes so that is not a viable material to be within the pipe [10].

Table 3: Dielectric strength of various materials

Material	Dielectric strength in MV/m
Air	3
SF_6	9.8
N_2	3.92
Distilled water	70
Benzene	163
Vacuum (200μPa)	40
Polypropylene (PP)	22
XLPE	27
CH_4	3

A question may be asked, that to keep things as similar as possible to the O&G industry, can methane (CH_4) be used as the dielectric. But this is impractical because methane is very flammable, and arcs formation is a possibility from a 1000 kV conductor. Table 3 shows that benzene has a high dielectric strength but is also too explosive.

Vacuum also has good dielectric strength, but it is hard to maintain a vacuum. Besides the pipe may collapse, the material in the pipe must have a higher pressure than the bottom of the Sunda shelf. A related information is that VCB (Vacuum Circuit Breaker) are only used for medium voltages like 11 kV or 33 kV and not for HV because of the possibility of leakage into the contact separation chamber especially via the seals of the moving contact. The third last material in Table 3 is PP (polypropylene plastic) with a dielectric strength of 22 has been used since the beginning of the electric industry and is gradually being replaced with XLPE because of the higher dielectric strength (27 from Table 3).

Therefore, the cheapest option is air and if the dielectric strength is insufficient, N_2 is the next best option. The difference in dielectric strength between N_2 and air is relatively small, but air has O_2 which can combust while N_2 is generally considered a non-combustible gas. It must be noted that O/H lines carry up to 1000 kV with separation distance between lines at about 15 m [11]. But at 7 atm the separation distance will be:

$$\frac{15m}{7\ atm} = 2.14\ m$$

That is between a line carrying 1000 kV to another line carrying 1000 kV. From 1000kV to 0V which is at the pipe's surface (sea water), the separation distance can reduce to half, or:

$$\frac{2.14\ m}{2} = 1.07\ m$$

Therefore, a pipe of 2 m diameter would be sufficient if 7 atm air is used as the dielectric.

The least flammable gasses are the Noble gasses, (He, Ne, Ar, Kr, Xe and Rn) [12]. But they are expensive to procure at such high amounts. Comparatively, N_2 is considered non-flammable because it cannot sustain combustion on its own even at extremely high

temperatures, which a 1000 kV electric arcs can create. The reason is that the triple bond between the two N is very strong. A tremendous amount of energy is required to break this bond. At very high temperatures and pressure the triple bonds between the two N can be weakened enough to participate in chemical reactions as in the Haber process where NH_3 is formed [13].

The advantage of joining the grids of these countries is to enable sharing of power. Similarly, Europe decided to utilize intermittent renewable energy as much as possible therefore the ENTSO-E (European Network of Transmission System Operators for Electricity) was joined and locked at 50 Hz and generates 670 GW [14]. With such a large grid, in case there is a sudden no wind situation over the large wind farm north of the UK, solar farms in Spain can back it up. So, if there is an ASEAN grid, a sudden cloud cover over a solar farm in Malaysia can be backed up by geothermal energy from Indonesia.

The ENTSO-E has a spinning reserve of 80 GW [15]. The spinning reserve can be explained as the pressing of the accelerator of the combustion engine a little extra. In case there is a sudden lack of supply compared to demand (as when there is a sudden cloud cover over a large solar farm or a sudden no wind situation over wind farms), extra DC is sent to the rotor of the rest of the generators, and immediately extra AC comes out of the stator coils. But with the extra DC in the rotor, it becomes a stronger electromagnet, the stator coils will also have extra AC current which also makes it a stronger electromagnet. This extra electromagnetic force attracting the rotor and stator will slow down the rotor from 50 Hz which will cause the protection system to trip the grid. But since the accelerator in this power station is already being pressed extra, there is enough mechanical power to make the rotor turn at 50 Hz despite the higher attraction between the rotor and stator. The speed of the rotor is controlled by the governor.

The reason the protection system must trip the grid when the rotor slows (frequency reduces) can be explained as two generators with three coils in the stator, namely the L1, L2 and L3 coils. When the rotor electromagnet passes L1 coil in one generator, the AC waveform for L1 wire will be its peak voltage. But if at that moment in the other generator, the electromagnet passes the L2 coil instead of L1, this generator will have the AC wave at below 0 V. But in the grid, L1, L2 and L3 wires are joined with 275 kV cables, therefore the first generator will have a peak voltage of:

$$\frac{275\ kV}{0.707} \approx 388\ kV$$

The second generator will have a voltage of about -30 kV. Therefore, the 275 kV O/H lines will have +388 kV from one generator and -30 kV from the second generator, therefore the wire will experience:

+388 kV-(-30 kV)=418 kV

This will blow up the smaller of the two generators. This means if in one generator, the rotor passes L1 coil, it must pass the L1 coil in all generators in the grid. This is called synchronizing of all generators.

The above scenario is true if all the generators are ICE (internal combustion engine) or coal steam turbines where the rotors turn at 50 Hz. But if the generator is hydroelectric, the rotation speed is slower than 50 Hz, therefore less poles in the stator are used to overcome it. Gas turbines on the other hand spin at a much higher speed than ICE, therefore more poles in the stator are used. But AC waves in all the generators must be synchronized before they can be joined to the grid. To understand this, it is useful to relate it to the formula for generators which is:

$$n_S = \frac{120f}{P} \quad (4)$$

where n_S = speed of the generator in RPM, f = frequency, p = number of poles.

Spinning reserve isn't solely for sudden drops in wind or solar generation; it's also crucial for maintaining grid stability during other unforeseen events, such as unexpected generator outages or transmission line failures. It is a must in case a power generating engine trips anywhere in the grid. The missing power from that generator cannot be just absent, it must be backed up and this is done by increasing the DC in the rotor solenoids in all the other generators and immediately extra AC comes out of the stator coils. In Sarawak, the spinning reserve or the extra pressing of all the accelerators is 30% of the total power output.

Malaysia's largest state, Sarawak, is a hydroelectricity hub due to its equatorial location, which ensures high and consistent rainfall, and the mountains along its Indonesian border. These two key factors for hydroelectric power—ample water flow from the abundant rain and significant head (height) from the terrain—are particularly pronounced in Sarawak. The state receives an average of 157 inches of annual rainfall, five times the 31-inch average of temperate countries. Sarawak's mountainous border with Indonesia makes it a rarity among equatorial nations, unlike Congo, Gabon, and Brazil, which lack similarly extensive elevated regions. Tanzania and Kenya are equatorial anomalies of a different kind; likely affected by the same factors that led to the desertification of the Sahara, they receive less rainfall than temperate countries.

Brazil has the third largest hydroelectric dam in the world but half of it is located in Paraguay due to the lack of high mountains in Brazil and half of the profit from the dam goes to Paraguay [16]. It must be noted that hydroelectric dams are the most profitable business in the world. For example, if the Bakun dam produces 2.4 GW

and sells its electricity at the rate it sells to households, which is $0.07 per kWh, the profit is:

$$\frac{2400\ MW\ X\ 24\ X\ 365\ X\ 0.07}{1000\ kW} = \$1{,}471{,}680{,}000$$

This means that ≈ USD 1.5 billion can be made in a year from that dam with an estimated cost of only the labor cost of the few people working on the dam which can easily be covered with about a million USD. Comparatively the few km long LNG (Liquified Natural Gas) plant in Bintulu, Sarawak makes about that much per year but has lots of expenses like purchasing gas and continuously changing parts. One manager of the LNG plant moved to the high-tech industry located in Kuching, Malaysia for 10 years. When he eventually left the high-tech industry to be a contractor for the LNG plant where he previously worked but could not recognize most parts as they were continuously upgraded over time. He eventually gave up on that venture [Ang, Hong Huat, personal communications, 16/2/2019].

Comparatively, a staff of the Batang Ai dam in Sarawak stated that it never failed over the 21 years he worked there and there was no change of parts at all [Dominic Lai, personal communications, 2/16/2015]. Dams are just too simple to fail; it is just water falling down and turning a Francis turbine and a shaft from this turbine goes up to spin a generator's shaft.

The economic potential of high-water flow was recognized relatively late in Southeast Asia. The construction of the first hydroelectric dam in Sarawak occurred only in the 1980s, a stark contrast to Brazil, which built its first in 1883. This early investment has positioned equatorial Brazil as the world's second largest hydroelectricity producer, after China.

Beyond its high rainfall and mountainous terrain, Sarawak's demographics and economic history further support its focus on hydroelectricity. Despite comprising 37% of Malaysia's land area, it accounts for only 8% of the national population, resulting in a low population density in its resource-rich regions that facilitates dam construction and water impoundment [17].

Historically reliant on timber harvesting and oil palm cultivation, Sarawak faces economic transitions. Timber is a declining industry due to dwindling old-growth forests. While oil palm has been significant, its long-term viability in Sarawak's elevated, less nutrient-rich soils is questionable. The increased fertilizer costs anticipated in subsequent planting cycles threaten its profitability. Therefore, the abundant and renewable energy potential of hydroelectricity offers a sustainable and increasingly attractive alternative for Sarawak's economic future.

Therefore, the state government planned to build hydroelectric dams as a future source of income and jobs for the people of Sarawak. While local electric utility staff initially expressed skepticism about power sufficiency, the subsequent availability of hydroelectricity unlocked unexpected economic opportunities. For example, the founder of the Bintulu aluminum factory leveraged World Bank financing due to the renewable power source, achieving remarkable financial success and becoming one of Malaysia's top five wealthiest individuals.

Despite its long history of oil drilling in Sarawak since 1910 and previous reliance on fossil fuels for its energy needs, Shell plc has adopted the LEA's electricity (which is 70% hydroelectric) due to the enhanced World Bank loan prospects and improved global profile associated with utilizing renewable energy.

3. Methodology and results

Numerous experiments were done in this research to utilize carbon steel pipes to measure the feasibility of suspending power cables in the middle of such pipes. Eddy current losses on the pipes were measured. But with the latest HDPE pipes, arching or eddy current losses will not be a concern. An O&G piping consultant based in Kuala Lumpur who was consulted about the feasibility of this research was very positive and stated that a HDPE carrying only 7 atm of air or N_2 can even last for 100 years [Soegiarto, Bennet, personal communications, 21/6/2023]. He also informed that HDPE O&G pipes are currently being used among a small percentage of pipes laid off the coast of Malaysia. With HDPE pipes, the possibility of arcing to the circumference can easily be eliminated. But this research is done assuming the long-established steel pipes will be used.

The experiments performed for this research is assuming the most economically viable method of transmitting power from Kuching to Singapore is used, which is using an AC cable suspended in an O&G pipe with air at 7 atm pumped within it. The air will be sent in the pipe carrying the electric cable and in Singapore the air will enter another pipe and be sent back to Kuching to be cooled and sent back into the first pipe.

The O&G industry has been using steel pipes since 1859, therefore most of the problems associated with it have been rectified. Using AC, the high cost (including maintenance) of the AC to DC converters can be avoided.

The problem with using steel pipe for this transmission system is that eddy current will be formed on the pipe.

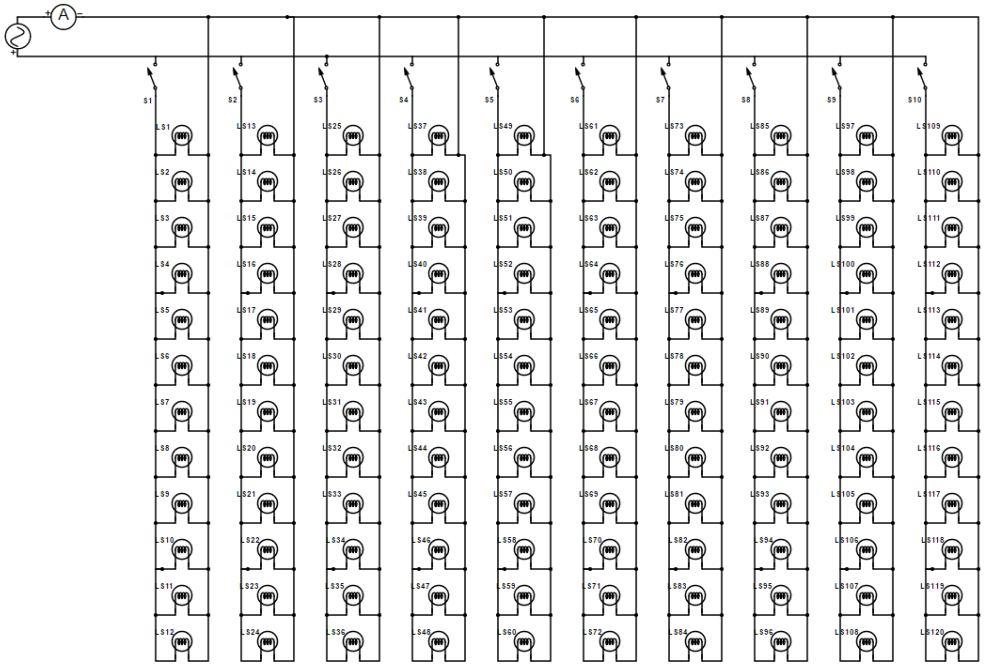

Figure 5: Connection of 120 incandescent bulbs; a 10 column X 12 rows was used. Each column had 12, 100 W incandescent bulbs. There is a switch at the beginning of each column.

In the experiment done in the lab, current varying from 0 A to 50 A was sent through bare wire of 2.5 mm^2 X 4 which is suspended in the middle of steel pipes and the heat generated on this pipe is measured using an infrared camera. Each 2.5 mm^2 wire has a current carrying capacity of 21A therefore 4 X 2.5 mm^2 can carry 21 X 4 = 84 A. The current applied to the cable was stepped up from 0A to 50 A, with each 5 A increment achieved by energizing additional columns of incandescent bulbs.

To prepare the cable, a length of about 2 m of 2.5 mm^2 cable was initially stripped of the PVC insulation by tying one end to a solid metal structure in the lab and using a wire stripper to strip it gradually. Then 4 X 2.5 mm^2 bare wires were placed next to each other and tied to the same solid metal structure in the lab. At the other end, the 4 X 2.5 mm^2 bare wires were clamped in the chuck of a drill and the drill chuck was clamped fast. Then as the drill is operated, the 4 X 2.5 mm^2 wires wound around each other in a tight helix.

The heat on the steel pipe is measured as the current sent through the cable is varied. Fig. 5 is a schematic of how all the 120, 100W incandescent bulbs are connected and Fig. 6 is its physical appearance. As shown in the schematic of Fig. 5, there is a switch at the top of each column, meaning each column can manually be switched making this setup a current generator to slowly increase current in the 4 X 2.5 mm^2 cable and the corresponding heat it generates on the steel pipe surrounding it can be measured and extrapolated. Fig. 7 is the setup to measure the heat on the steel pipe surrounding the cable.

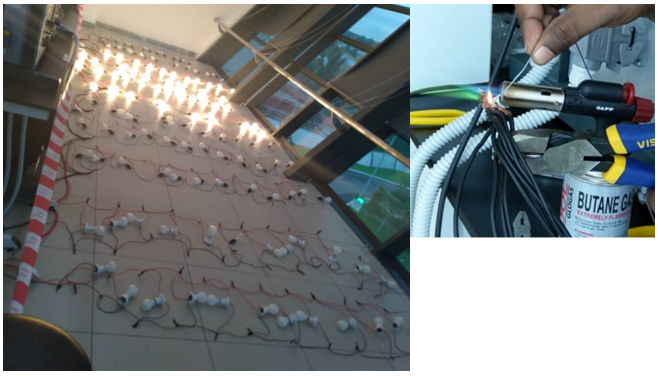

Figure 6: The load of incandescent bulbs connected in parallel with each parallel row individually switchable

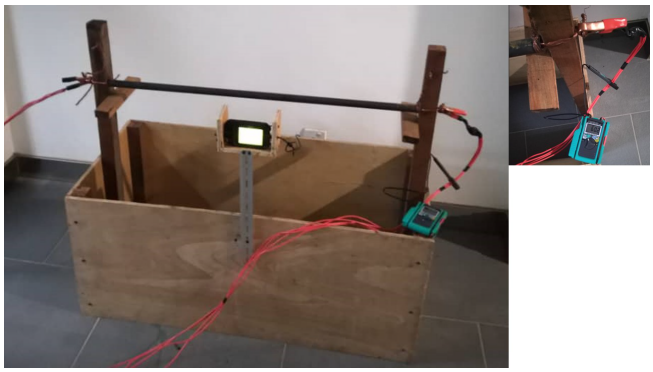

Figure 7: The setup used to determine the heat generated on the pipe

Fig. 6 right image depicts how 8 X 2.5 mm^2 wires are soldered. A butane gas flamer was used to heat the wires to solder the joint. Only the end of the joint can be flamed, and the heat will flow down, and it will be hot enough to melt solder wire. If the whole joint is flamed, it was observed that solder will not stick onto the joint. An explanation for this is that the Cu turned to CuO which is light orange in color. It must be noted that heated Cu is

one of the most colorful metals ranging from light orange, which will gradually turn to black as it turns to fully CuO and eventually become green as sulfur enters it. This is why the Cu Statue of Liberty in NY is currently green. An electric soldering iron cannot generate enough heat to solder 8 X 2.5 mm^2 wire joints. The same method is used in the joining of large wires in the construction of very large motors but using O_2 acetylene instead of a butane torch.

Table 4 is the results obtained, and Fig. 8 are the results depicted as a graph. The legend of the different colors at the bottom of the chart indicates the diameter of the pipes surrounding the bare Cu cable carrying current which was varied from 0 A to 50 A in steps of 5A. Obviously the line graph for the smallest pipe with Ø = 1.11 cm goes straight up indicating it is the hottest and the black line graph has the lowest slope because of the bigger pipe of Ø = 4.45 cm surrounding the conductor. For this pipe, the heat on the pipe just went just 6^{o}C above ambient. Using Excel to extrapolate the temperature rise to 1000 A, the temperature if Ø = 4.45 cm pipe is used will be 187^{o}C. But if the diameter of the pipe is extrapolated to Ø = 2 m with the cable within carrying 1000 A, there will be zero detectable heat or eddy current.

This heat data is extrapolated to 1000 A which is the loading currently suggested in the media for the proposed XLPE submarine cable from Kuching to Singapore.

Table 4: The results of the sending AC current in a cable suspended within a pipe

Pipe Radius (cm)	Current (A)										
	0	5	10	15	20	25	30	35	40	45	50
	Temperature (^{0}C)										
1.11	30	30.1	30.3	31.1	33.0	36.5	39.7	44.4	48.7	53.6	57.6
1.59	30	30.1	30.1	31.1	31.6	32.3	33.5	35.5	38.5	42.1	44.7
2.22	30	30.1	30.1	30.1	30.9	32.4	33.5	35.3	36.7	40.0	41.4
2.54	30	30.1	30.1	30.1	31.3	32.4	33.3	34.9	36.4	39.5	41.3
3.18	30	30.1	30.2	30.2	30.9	32.3	33.0	33.7	35.1	36.3	37.5
3.81	30	30.0	30.1	30.1	30.2	31.4	32.8	33.6	34.7	36.0	37.3
4.45	30	30.1	30.1	30.2	30.3	30.5	31.6	32.8	33.9	35.2	36.0

Some other researchers, even IEEE reviewers, state that the heat measured on the pipe surrounding the cable is due to Joule heating. But Fig. 9 and Fig. 10 illustrate that the heat on the pipe is due to eddy current and not Joule heating. The infrared camera used is FLIR C2 which takes two pictures consecutively, a picture of the infrared waves emitted by objects and a picture of the white light emitted as depicted in the left and right image of Fig. 9.

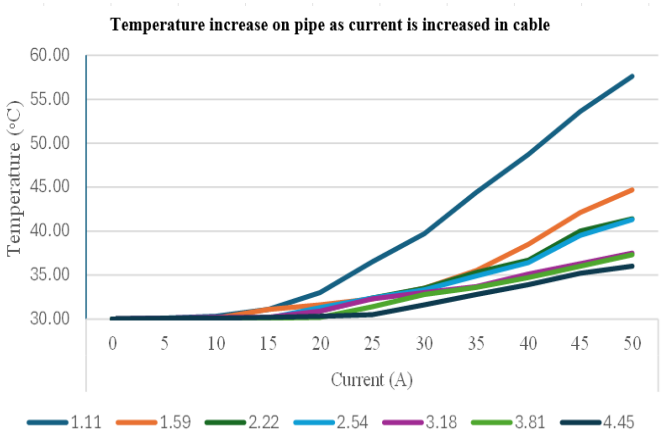

Figure 8: Temperature rise on the pipe with diameters specified by different colors at the bottom of the chart, as current in the cable suspended within the pipe is increased

In the infrared image of Fig. 9, the steel pipe on the right has (2.5 mm^2 X 4) L wires and (2.5 mm^2 X 4) N wires or a total of 8 wires are within the steel pipe. A current of 50 A flows through L and 50 A returns through N wires. On the steel pipe on the left, there are (2.5 mm^2 X 4) X 2) = 8 L wires within the steel pipe. The L wires were rolled through the pipe twice. It can be observed in the infrared image of Fig. 9 that the right steel pipe is at the highest temperature in the scale of temperatures located in between the infrared and white light image. And the steel pipe with the 4 L and 4 N wires which the student is pointing at is almost at ambient temperature.

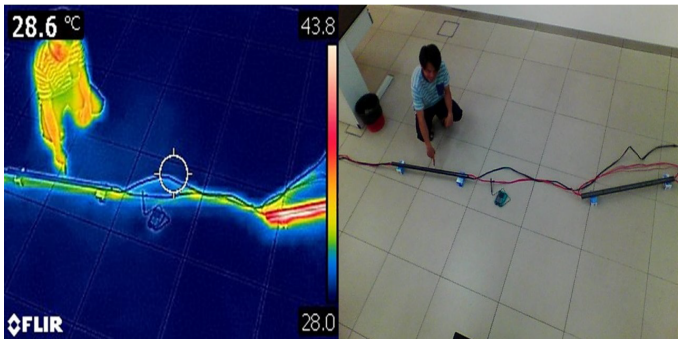

Figure 9: Eddy current experiment

If Joule heating is the cause of the heat generated on the steel pipe, both pipes should have the same heat because both steel pipes have (8 X 2.5mm^2) wires and the current flowing in the wires in both pipes is 100A.

To understand what is happening, assume the pipe is only one wavelength long. Fig. 10 depicts that current is flowing as a sine wave in the L wires. But the current in the N wires is flowing in a sine wave with opposite amplitude. Therefore, the magnetic field generated by the L wires will superimpose the magnetic field generated by the N wires. Therefore, there is ≈ zero remaining magnetic field (assuming all the factors affecting conductivity are the same) within the pipe and therefore

≈ zero eddy current generated on the steel pipe and therefore ≈ zero heat generated on the steel pipe.

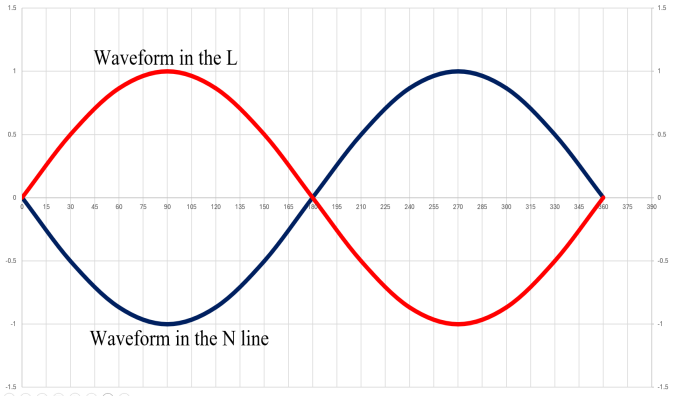

Figure 10: The L and N wire magnetic fields are opposite of each other superimposing each other resulting in zero net magnetic field and thereby ≈ zero eddy current and heat on the left pipe

Steel pipes were chosen for this experiment because, at the outset of this research, the prevalence of HDPE in a small percentage of oil and gas (O&G) pipes was unknown. The dielectric strength of air at 7 atm is sufficient for this setup. Furthermore, a safety system could be implemented to shut down the line in the event of air pressure decreasing.

Steel was used by O&G because of its strength and durability to withstand up to 1000 atm pressure. Its other advantages are the versatility due to the big industrial base and machines to modify it. It is also easily available, being the fourth most abundant element on the earth's crust.

Distinguishing the eddy currents induced in the pipe from Joule heating within the cable is crucial. Joule heating arises when the current surpasses the cable's carrying capacity, as shown in Table 2 (e.g., 21A for a 2.5 mm² wire in conduit). Exceeding this limit results in resistive heating, a principle employed in materials like nichrome, known for their high-temperature tolerance despite significant current flow [18]. This heating stems from collisions between electrons and ions in the conductor, increasing their kinetic energy and manifesting as a temperature rise. To isolate eddy current effects on the pipe in this experiment, the maximum applied current to the cable was 50A, significantly below its 84A carrying capacity for the 4 X 2.5mm² wires.

To physically understand eddy current, one can use the right hand shaped according to the Fleming's Right Hand Rule (FRHR). FRHR is defined as the thumb (F) pointing at the direction of movement of the magnet; normally taught in schools as F = Force. The index finger is pointing in the direction of the magnetic field (B) and the middle finger is pointing in the direction of the generated current (I).

A magnet with 10 magnetic field lines can be represented as a hand pointing as the FRHR passes a wire below it at a right angle. What the wire will see when the magnet is far away is initially 0 magnetic field line. Then it will see 2, then 3, 4, 5, 6, 7, 8, 9, then 10 field lines as the magnet is right above the wire. Therefore, what the wire will see is a varying Field density. So instead of defining the F as Force as is taught in high schools, it is better to define it as varying Field density (which still uses F). Even if the strongest magnet in the world (which has the highest magnetic field density) is placed just above the conductor but not moved, there will be no current generated in the conductor below it. In other words, only a variable Field density enables current to be generated in the conductor below it.

To understand how eddy current is generated in a wire carrying AC current, one can use the right hand shaped as FRHR moving up and down over the right hand's lower arm. The FRHR represents a single electron. In AC, electrons move back and forth because, if the current is from the L1 phase within the generator. As the L1 phase coil in the generator's stator is passed by the N pole of the rotor solenoid (which is energized with DC), current will travel to the loads of the country. And when this N pole passes the anticlockwise coil located at the bottom of the stator, current will come back from the loads of the country. Thus, each electron moves back and forth in an AC wire. But as the rotor solenoid's N pole passes the top clockwise coil, the solenoid's S pole will pass the anticlockwise coil located at the stator's bottom. This will provide double the current for the load.

As the right hand which is shaped as the FRHR moves back and forth over the left-hand's lower arm. Assume a single electron has 10 magnetic field lines. At the top and bottom of the left hand's lower arm (end of the back-and-forth movement), there will be 10 magnetic fields lines around the electron since the speed of the electron is zero; just as the speed of a stone thrown up will experience zero speed before coming down due to gravity. But as it moves to the center of the left lower arm, the speed of the electron will increase till it is at a maximum at the center of the left lower arm. The electron will travel so fast that the magnetic field lines will linger even if the electron has passed a particular point in the wire. Therefore, at the center of the lower left arm, there will be a maximum number of field lines and at the two ends there will only be 10 field lines. Meaning there is a varying Field density (F of the FBI is present) as an electron moves back and

forth within a point in a wire. Since an electron is a magnet which already has B, I will be generated. It can be observed from the FRHR that the current generated will be from the center of the wire to the outside. This current generated is termed as eddy current and it causes all flow of electrons in an AC wire to be only at the outer diameter; this is termed as skin effect. This is why in a typical O/H line, the structure is to have seven strands of steel surrounded by four layers of aluminum. Aluminum is brittle while steel will provide strength. This will enable the towers to be spaced further thereby saving cost since the cost of the towers is one of the most expensive portions of O/H line cost. The current does not flow through the steel wires because of the skin effect.

For DC transmission using O/H lines, even if the DC current is of very high magnitude, thereby making the magnetic field lines density very high, the magnetic Field density is not varying therefore there is no F and therefore no I generated. Therefore, the skin effect does not happen in DC lines so the whole cross-sectional area of the cable can be utilized for transmission. This is why DC lines can typically carry 100% or two times the current carried by AC lines. It must be noted that for O/H lines, steel reinforcement at the center must still be used to enable the towers to be spaced as far as AC towers, but despite that if DC is used, double the current can be carried [19].

If a steel pipe is placed around a conductor carrying AC, there will be a continuous eddy current generated which will push out the electrons flowing in the cable to the skin, plus the same magnetism will generate eddy current flow in the pipe surrounding the cable. This generated current has no polarity and will therefore behave like hurricanes of current within the steel pipe which will generate heat.

In the procedures of laying 11 kV and above U/G cables, the cable must be placed within a steel pipe if the cable passes a drain or under a road. But if only one single Φ cable is placed in a steel pipe, it can be observed that it will get hot. Experiments were done to determine if the eddy current generated is a linear function of the current sent through the conductor. Initially voltage was varied in the experiment but there was no heat generated in the steel pipe surrounding the conductor. This is further proof that voltage is a measure of electric field and current is a measure of magnetic field. The two fields are at a right angle to each other. An electric field is a field which will move a polarized ion, a magnetic field has no effect on a polarized ion. A voltmeter measures the magnitude of the electric field while an ammeter measures the magnitude of the magnetic field.

The eventual objective of this research is to send 1 GW of power between Kuching and Singapore using HVDC suspended at the center of steel pipes which are currently used by the O&G industry. Each pipe is 11.5 m and at the end of each pipe three insulators can be made to suspend the power cable at the star point as shown in Fig. 1. Air can be pumped to the pipe and another pipe will bring back the air or N_2 from Sarawak to be refrigerated and recycled back to the pipe carrying the conductor. Air or N_2 is mentioned because N_2 could be too expensive for this 700 km pipe; further research on choosing air or pure N_2 is needed as the dielectric. Barges must be long enough to stretch the drum of cable on the barge. Then an 11.5 m steel pipe is brought to the beginning of the cable and dragged to the other end of the barge. A star point shaped plastic insulator which will enable suspending the cable at its star point is then dragged from the beginning of the cable to the other end and fitted into the pipe. The three plastic insulators need to have a plastic base to hold it together as it is pushed into the pipe. Therefore, as shown in Fig. 11, a cylindrical plastic base is needed to hold the three insulators together. Then binding wire is used to fasten the 500 mm^2 cable to the three insulators. This process is repeated with a second pipe dragged from the beginning of the cable to the other end of the barge. And the two steel pipes are welded. The plastic insulators must be placed far enough within the pipe such that the heat from the welding does not melt it.

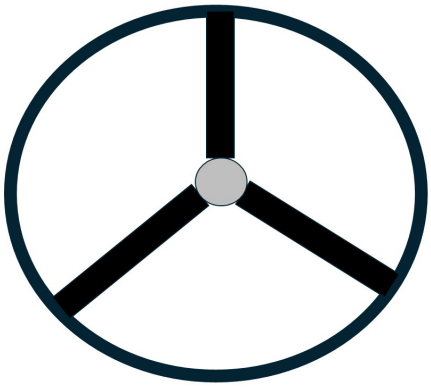

Figure 11: The star point insulator with a cylindrical base to hold it together

Research done so far indicates that air at about 7 atm of air should be sufficient dielectric for the 1000 kV transmission. The Sunda Shelf shown in Fig. 3 has an average depth of 50 m. At this depth the pressure is:

$$P = D\ X\ g\ X\ d \tag{5}$$

$$P = 1024\frac{kg}{m3}X\ 9.8\frac{m}{s2}X\ 50m = \ 501{,}760\ pa$$

$$\mathrm{P} = 4.9583\ atm\ \approx 5\ atm$$

Where P = Pressure, D = density of water, g = gravity, d = depth. Therefore, at the seabed, 5 atm is exerted on the steel pipe. The O&G industry typically sends gas at 10-1000 atm. Obviously, the pressure within the pipe needs to be above the pressure the sea water exerts upon the pipe. Therefore, air needs to be sent into the pipe at 7 atm. This way, in case of a leak, there will be positive pressure out of the point of leak. The point of leak will most likely be at the joint point of the steel pipe. The joint point of the pipe where steel pipe is joined by welding could be done improperly thereby enabling water seepage. Therefore, it is highly recommended that robotic welding be used to provide consistency in the welding process.

For HDPE pipes the joints are done with heat fusion. As water seeps within the pipe, there will be a 1000 kV to 0V (sea water) arcing. For HDPE pipes there will be a cover over the joint as shown in the HDPE water pipe shown on Fig. 12.

Figure 12: A HDPE pipe joint

The dielectric strength of the air should be sufficient to withstand arcing. The choice of 7 atm is because the pumps to build up such pressure have already been built by the O&G industry and a new pump need not be developed specifically to send electricity within a pipe. This is assuming N_2 and CH_4 follow the ideal gas law of equation (4).

$$PV = nRT \tag{6}$$

The dielectric strength of air and N_2 at 1 atm is around 3 MV/m. The steel or HDPE pipes used by the O&G range can range from Ø = 914 - 2000 mm. If a Ø = 2000 mm is used, the dielectric strength of the air or N_2 from the center of the pipe to the pipe will be:

7 atm X 3 MV/m=21,000 MV/m

For this design, the conductor will be having 1000 kV, therefore the protection from arching needed is only 1000 kV. But at 7 atm, the smallest pipe currently used by the O&G industry can be used which will provide a dielectric strength of the N_2 of:

$$7\ atm\ X\ \frac{914mm}{1000}\ X\ 3\frac{MV}{m} = 19{,}194\ MV/m$$

It must be noted that if DC is used, the breakdown voltage is two times higher meaning that it will be two times harder for arcs to happen with DC. This is because when AC is used there is a space charge accumulation around imperfections in the insulator. These space charges can create fields and cause breakdowns easier.

With a dielectric strength of 19,194 MV/m even AC can be used but to synchronize the grid of Sarawak and Singapore will be a challenge, the safest way to synchronize the two grids is to shut down all power in Sarawak for a probably half a day and restart all engines with Singapore's frequency. Many claim that modern equipment can handle synchronization. But if synchronizing the grid of Sarawak and Singapore fails by even a millisecond, the result can be catastrophic. Note that the interconnection is 1000kV. One cycle is 20 ms. Even if the synchronizing is off by 5 ms a phase I of Singapore could be at 0 V at one moment of time, but Sarawak will be at peak voltage divided by two because the sine wave will be quarter cycle up from 0 V:

$$\frac{1000\ kV}{0.707\ X2} = 7072\ kV$$

Which will be high enough to destroy lots of equipment in the Sarawak grid. This potential loss is far worse than shutting down power of the Sarawak grid and slowly synchronizing each generator to Singapore's frequency. It is not practical to shut down Singapore's power since Singapore's economy is larger than Malaysia's economy of 13 states where Sarawak is only one state.

HVDC is currently used in joining grids of different frequencies. There is a HVDC line utilized to join the grids of West Malaysia and Thailand. HVDC towers and lines cost 30% less than HVAC towers and lines.

4. Conclusion

This work was done to facilitate the aspiration of the government to send 1 GW of power from Sarawak to Singapore over 700 km. Justifying this research is the fact that it is highly unlikely that the currently planned XLPE insulated conductor will be able achieve 1 GW transmission over 700 km simply because there is no vent for the Joule heating in the cable. The insulation must be quite thick because of the possibility of a 1000 kV in the cable to 0 V of the sea water and therefore this insulation will trap the Joule heating of the cable.

The proposed system in this research is because Sarawak has been drilling oil since 1910 and there is a vast network of submarine O&G pipes north of Sarawak.

There are also lots of very eager contractors and consultants within Sarawak who can easily lay a O&G pipe between Kuching to Singapore with a conductor suspended at its center. Air will be pumped within this pipe and another pipe will bring back the air to Kuching to be cooled and sent back to Singapore. This air will be at 7 atm because the O&G industry has already built pumps to pressurize the gas to that pressure.

A key finding of this research was the presence of HDPE pipes in a small percentage of existing submarine O&G infrastructure. While this experiment assumed the use of traditional steel pipes, which have been employed by the O&G industry since 1859, the potential for using HDPE pipes presents a significant advantage: it would substantially reduce concerns about arcing from the 1000 kV cable to the 0 V seawater. The primary limitation of HDPE pipes in this context, however, is their relative novelty and thus, their less extensive time-tested history within the O&G industry compared to steel.

HVDC is a good choice for this cable for two reasons. Firstly, the Singapore grid is at a different frequency from the Sarawak grid and a HVDC line can connect two different frequency grids without the need for synchronizing. Secondly, HVDC can carry current without eddy current loss. Only Joule heating loss is possible with HVDC. But the AC to DC converter is very expensive, including its maintenance cost.

The aim in this work is to study the feasibility of using a Ø = 2 m pipe and 1000 GW (1000 A at 1000 kV) which is the current value broadcasted in the media for the proposed XLPE insulated submarine line between Sarawak and Singapore.

The next step in this research is to get research funding to lay about 1 km of steel pipes and run 11 kV of power within it since that is the lowest HV used before LV voltages for domestic consumption in Sarawak.

Acknowledgement

This research was sponsored by a grant from University of Technology Sarawak (UTS) with reference: UTS/Research/<4/2017/14>(01)

References

[1]. P. Karunakaran et al., "Electricity transmission under South China Sea by suspending cables within pipes," in Proc. IEEE Int. Conf. Emerging Trends in Engineering, 2020, pp. 1–5. doi: 10.1109/INCET49848.2020.9154119.

[2]. R. Tricker, Wiring Regulations Pocket Book. Routledge, 2021. doi: 10.1201/978100316170.

[3]. C. S. M. McGrath et al., "Pleistocene Sunda Shelf submersion-exposure cycles initiate vegetation-Walker Circulation feedback," Geology, vol. 51, no. 11, pp. 1053–1056, 2023. doi: 10.1130/G51412.1.

[4]. L. Zhang, Y. Yin, and W. Shi, "Research on the lightning protection of UHV long-distance GIL system," in Proc. 8th Asia Conf. Power and Electrical Eng. (ACPEE), 2023, pp. 1163–1167. doi: 10.1109/ACPEE57237.2023.10103681.

[5]. P. Argaut, "Underground cables," in Springer Handbook of Power Systems, 1st ed., Springer, 2021, pp. 759–866. doi: 10.1007/978-981-32-9938-2_10.

[6]. J. G. Theis, G. R. Werner, T. G. Jenkins, and J. R. Cary, "Computing the Paschen curve for argon with speed-limited particle-in-cell simulation," Phys. Plasmas, vol. 28, no. 6, 2021. doi: 10.1063/5.0051095.

[7]. P. Billen, B. Maes, M. Larrain, and J. Braet, "Replacing SF_6 in electrical gas-insulated switchgear: Technological alternatives and potential life cycle greenhouse gas savings in an EU-28 perspective," Energies, vol. 13, no. 7, p. 1807, 2020. doi: 10.3390/en13071807.

[8]. Y. S. Zulkarnain et al., "The dielectric power of mixed gas insulation of SF_6–CO_2 and SF_6–N_2," in Proc. Int. Seminar on Intelligent Technology and Its Applications (ISITIA), 2022, pp. 355–359. doi: 10.1109/ISITIA55981.2022.9854746.

[9]. U. Riechert, "Compact high voltage direct current gas-insulated systems," in Proc. IEEE Int. Conf. High Voltage Engineering and Application (ICHVE), 2020, pp. 1–4. doi: 10.1109/ICHVE50860.2020.9280047.

[10]. R. Arora and W. Mosch, "High Voltage and Electrical Insulation Engineering". John Wiley & Sons. doi: 10.1002/9781119568940.

[11]. H. Liang and Q. Xie, "Shaking table test on 1000 kV UHV transmission tower-line coupling system," Structures, vol. 27, pp. 650–663, 2020. doi: 10.1016/j.istruc.2020.06.017.

[12]. D. Porcelli, C. J. Ballentine, and R. Wieler, "An overview of noble gas geochemistry and cosmochemistry," Rev. Mineral. Geochem., vol. 47, no. 1, pp. 1–19, 2002. doi: 10.2138/rmg.2002.47.1.

[13]. S. Kim, F. Loose, and P. J. Chirik, "Beyond ammonia: nitrogen-element bond forming reactions with coordinated dinitrogen," Chem. Rev., vol. 120, no. 12, pp. 5637–5681, 2020. doi: 10.1021/acs.chemrev.9b00705.

[14]. H. Zsiborács, A. Vincze, G. Pintér, and H. Baranyai, "The accuracy of PV power plant scheduling in Europe: an overview of ENTSO-E countries," IEEE Access, vol. 11, pp. 74953–74979, 2023. doi: 10.1109/ACCESS.2023.3297494.

[15]. R. Bovera, D. Falabretti, and M. Merlo, "Data-driven evaluation of secondary-and tertiary-reserve needs with high renewables penetration: The Italian case," Energies, vol. 14, no. 8, p. 2157, 2021. doi: 10.3390/en14082157.

[16]. V. Fruet, D. Campos, and L. Caridad, "Itaipu Binational Dam: A quantitative analysis of the economic and social impacts in Paraguay. Successful or not?", SAGE Open, vol. 13, no. 4, p. 21582440231216820, 2023. doi: 10.1177/21582440231216820.

[17]. P. Karunakaran et al., "Eddy current versus Joule heating effects for a cable suspended in an iron pipe," in Proc. IEEE Int. Conf. INOCON, 2020. doi: 10.1109/INOCON50539.2020.9298266.

[18]. G. L. Zhunkovskii, O. N. Grigoriev, and D. V. Vedel, "Interaction of titanium diboride with nickel and Ni–20% Cr alloy (nichrome),", Powder Metall. Met. Ceram., vol. 60, no. 9, pp. 586–596, 2021. doi: 10.1007/s11106-021-00277-y.

[19]. P. Karunakaran, Electrical Power Simplified. AuthorHouse, 2015. ISBN: 978-1504965422.

Pashobh Kumar Karunakaran earned his bachelor's and master's degrees from South Dakota State University, USA. He then got his PhD from Universiti Sarawak Malaysia (UNIMAS). He is currently an Associate Professor in Electrical Engineering in University of Technology Sarawak (UTS), Sibu, Malaysia.

Prashobh has published 86 papers, published two books and achieved seven awards for research works.